Mon. Not. R. Astron. Soc. **000**, 000–000 (0000) Printed 24 October 2016 (MN LATEX style file v2.2)

The SILCC project — IV. Impact of dissociating and ionising radiation on the interstellar medium and Hα emission as a tracer of the star formation rate

Thomas Peters[1⋆], Thorsten Naab[1], Stefanie Walch[2], Simon C. O. Glover[3], Philipp Girichidis[1], Eric Pellegrini[3], Ralf S. Klessen[3,4], Richard Wünsch[5], Andrea Gatto[1], Christian Baczynski[3]

[1] *Max-Planck-Institut für Astrophysik, Karl-Schwarzschild-Str. 1, D-85748 Garching, Germany*
[2] *I. Physikalisches Institut, Universität zu Köln, Zülpicher Strasse 77, D-50937 Köln, Germany*
[3] *Universität Heidelberg, Zentrum für Astronomie, Institut für Theoretische Astrophysik, Albert-Ueberle-Str. 2, D-69120 Heidelberg, Germany*
[4] *Universität Heidelberg, Interdisziplinäres Zentrum für Wissenschaftliches Rechnen (IWR), D-69120 Heidelberg, Germany*
[5] *Astronomical Institute, Academy of Sciences of the Czech Republic, Boční II 1401, 141 31 Prague, Czech Republic*

arXiv:1610.06569v1 [astro-ph.GA] 20 Oct 2016

24 October 2016

ABSTRACT

We present three-dimensional radiation-hydrodynamical simulations of the impact of stellar winds, photoelectric heating, photodissociating and photoionising radiation, and supernovae on the chemical composition and star formation in a stratified disc model. This is followed with a sink-based model for star clusters with populations of individual massive stars. Stellar winds and ionising radiation regulate the star formation rate at a factor of ~ 10 below the simulation with only supernova feedback due to their immediate impact on the ambient interstellar medium after star formation. Ionising radiation (with winds and supernovae) significantly reduces the ambient densities for most supernova explosions to $\rho < 10^{-25}\,\mathrm{g\,cm^{-3}}$, compared to $10^{-23}\,\mathrm{g\,cm^{-3}}$ for the model with only winds and supernovae. Radiation from massive stars reduces the amount of molecular hydrogen and increases the neutral hydrogen mass and volume filling fraction. Only this model results in a molecular gas depletion time scale of 2 Gyr and shows the best agreement with observations. In the radiative models, the Hα emission is dominated by radiative recombination as opposed to collisional excitation (the dominant emission in non-radiative models), which only contributes $\sim$ 1–10 % to the total Hα emission. Individual massive stars ($M \geqslant 30\,\mathrm{M_\odot}$) with short lifetimes are responsible for significant fluctuations in the Hα luminosities. The corresponding inferred star formation rates can underestimate the true instantaneous star formation rate by factors of ~ 10.

1 INTRODUCTION

Massive stars (O and B stars with masses in excess of $8\,\mathrm{M_\odot}$) dominate the energy output of newly formed stellar populations. Most of the energy is emitted in the form of (ionising) radiation, followed by supernova explosions (about one order of magnitude less) and stellar winds (another order of magnitude less). Photoionising radiation (photon energies larger than 13.6 eV) is a major source of ionised hydrogen and drives the formation of H II regions (e.g. Whitworth 1979; Dale et al. 2005; Peters et al. 2010; Walch et al. 2012; Geen et al. 2015), which cool by Lyman α radiation. This effect is significant although, energetically, the coupling of gas and radiation is usually very inefficient (less than 0.1 % of the emitted energy in the Lyman continuum can be converted into kinetic energy, see e.g. Walch et al. 2012). Photoionising radiation is also a major source for Hα emission, which is used as one of the major tracers for star formation in galaxies at low and high redshifts (e.g. Kennicutt 1998; Förster Schreiber et al. 2009)

How radiation couples to the surrounding gas depends on the wavelength of the radiation, and energies below the Lyman continuum also have to be considered. For example, photoelectric heating of dust (photon energies of 5.6 eV – 13.6 eV) is the dominant heat source in the interstellar medium (ISM, Draine 1978). It can lead to temperatures of a few 10^3 K and contribute to the formation of the warm, neutral component of the ISM (WNM), where the fine-structure lines [C II] and [O I] are the main coolants. In addition, photodissociating radiation (photon energies of 11.2 eV – 13.6 eV) will destroy molecular hydrogen and change the abundance ratios. Photoionising radiation from massive stars can heat the ISM to temperatures up to $\sim 10^4$ K and impacts the chemistry and thermodynamics of the cold neutral, the warm neutral, and the warm ionised

© 0000 RAS

medium directly. The cold neutral medium (in particular molecular hydrogen) is the fuel for new stars and correlates well with the star formation rate (SFR) of galaxies at low as well as high redshifts (e.g. Bigiel et al. 2008; Tacconi et al. 2010).

Supernovae and to some degree stellar winds are energetic enough to shock-heat the ISM to temperatures of $\sim 10^6\,\mathrm{K}$ and generate hot gas (Weaver et al. 1977; Ostriker & McKee 1988) for which bremsstrahlung emission becomes the dominant cooling radiation. It has been argued that supernova-driven shocks play a significant role for driving ISM turbulence (Mac Low & Klessen 2004), accumulate dense and cold gas and form a hot, possibly volume-filling, medium which is responsible for driving galactic outflows (see e.g. Joung & Mac Low 2006).

The emission of ionising radiation, stellar winds and supernova explosions are therefore the dominant sources that determine the chemo-thermodynamic properties of the ISM. They should all be considered in modern attempts to improve the numerical modelling towards a more complete model of the ISM.

Significant progress has been made on individual aspects. Simulations focusing on the impact of supernovae on ISM structure (Kim & Ostriker 2015a; Walch & Naab 2015; Martizzi et al. 2015) indicate a regulation of star formation and vertical disc structure in models limited to momentum injection (e.g. Kim & Ostriker 2015b) as well as the formation of galactic outflows in simulations including the formation of a hot phase (e.g. Korpi et al. 1999; Joung & Mac Low 2006; de Avillez & Breitschwerdt 2004; Henley et al. 2015; Peters et al. 2015; Girichidis et al. 2016). Stellar winds impact the ambient ISM structure, possibly terminating gas accretion onto star-forming regions and thereby regulating the local efficiency of star formation (Gatto et al. 2016). They also change the conditions for subsequent supernova explosions by reducing the ambient gas densities making energy deposition from supernovae more efficient. Ionising radiation has a similar effect by heating the dense gas phase in star-forming regions to $10^4\,\mathrm{K}$, injecting momentum into the ISM, and driving turbulence locally (Peters et al. 2008; Gritschneder et al. 2009; Geen et al. 2015).

In this paper we present the first chemo-dynamical numerical models sequentially including all the above processes—ionising radiation followed with the radiation transfer code `Fervent` (Baczynski et al. 2015), stellar winds, and supernova explosions—in combination with a sink particle-based star cluster formation model (Gatto et al. 2016). We investigate a small region of a galactic disc with solar neighbourhood-like properties in the stratified disc approximation. The model is combined with a chemical network to follow the evolution of molecular, neutral and ionised gas in the presence of an external radiation field (see Walch et al. 2015 for details on the SILCC project, https://hera.ph1.uni-koeln.de/∼silcc/). In this paper we do not investigate the effect of non-thermal ISM constituents like magnetic fields or cosmic rays.

The paper is organised as follows. In Section 2 we present an overview of the simulations followed by a discussion about the energy budget of wind, radiation and supernova feedback processes (Section 3). A qualitative discussion of the simulation results (Section 4) is followed by quantitative analyses of the star cluster properties (Section 5), energy input (Section 6), mass fraction in different ISM phases (Section 7), depletion times (Section 8) and volume filling fractions (Section 9). The origin of Hα emission is discussed and interpreted in in Sections 10, 11, and 12. We conclude in Section 13.

2 SIMULATIONS

We use the adaptive mesh refinement code `FLASH` 4 (Fryxell et al. 2000; Dubey et al. 2009) to run kpc-scale stratified box simulations. We employ a stable, positivity-preserving magnetohydrodynamics solver (Bouchut et al. 2007; Waagan 2009; Waagan et al. 2011). Self-gravity is incorporated with a Barnes-Hut tree method (R. Wünsch et al. in prep.). The simulated boxes have dimensions $0.5\,\mathrm{kpc} \times 0.5\,\mathrm{kpc} \times 10\,\mathrm{kpc}$. The box boundaries are periodic in the disc plane (x and y directions). We allow the gas to leave the simulation box in the vertical (z) direction, but prevent infall into the box from the outside (diode boundary conditions). The highest grid resolution is $\Delta x = 3.9\,\mathrm{pc}$.

The gravitational force of the stellar component of the gas is modelled with an external potential. We assume an isothermal sheet potential with a stellar surface density $\Sigma_* = 30\,\mathrm{M_\odot\,pc^{-2}}$ and a vertical scale height $z_\mathrm{d} = 100\,\mathrm{pc}$. These parameters were chosen to fit solar neighbourhood values. The gas is set up with a surface density $\Sigma_\mathrm{gas} = 10\,\mathrm{M_\odot\,pc^{-2}}$. In z-direction, the gas follows a Gaussian distribution with a scale height of 60 pc. We do not include magnetic fields in the simulations presented in this paper. More information on the initial conditions and the setup of the simulations can be found in Walch et al. (2015) and Girichidis et al. (2016).

Heating and cooling processes, as well as molecule formation and destruction, are treated with a time-dependent chemical network (Nelson & Langer 1997; Glover & Mac Low 2007a,b; Glover et al. 2010; Glover & Clark 2012). The network follows the abundances of free electrons, H^+, H, H_2, C^+, O and CO. Warm and cold gas primarily cools via Lyman-α cooling, H_2 ro-vibrational line cooling, fine-structure emission from C^+ and O, and rotational emission from CO (Glover et al. 2010; Glover & Clark 2012). In the hot gas, we also take the electronic excitation of helium and of partially ionised metals into account following the Gnat & Ferland (2012) cooling rates. We assume X-ray ionisation and heating rates based on Wolfire et al. (1995) and a cosmic ray ionisation rate $\zeta = 3 \times 10^{-17}\,\mathrm{s^{-1}}$ following Goldsmith & Langer (1978). Furthermore, we assume a diffuse interstellar radiation field $G_0 = 1.7$ (Habing 1968; Draine 1978) and include the effect of heating from the photoelectric effect using the prescription by Bakes & Tielens (1994). Shielding by dust as well as molecular self-shielding is modelled with the `TreeCol` method (Clark et al. 2012, R. Wünsch et al. in prep.). The assumed metallicity is solar. For more information on the chemical network and our description of heating and cooling see Gatto et al. (2015) and Walch et al. (2015).

Star clusters form dynamically and are modelled using sink particles (Federrath et al. 2010). The accretion radius of the sink particles is $r_\mathrm{acc} = 4.5 \times \Delta x = 17.58\,\mathrm{pc}$. The sink particles have a threshold density of $\rho_\mathrm{thr} = 2 \times 10^{-20}\,\mathrm{g\,cm^{-3}}$. All gas within r_acc that is above ρ_thr, bound to the sink particle and collapsing towards the centre will be removed

from the grid and accreted onto the sink particle. As soon as we have accreted $120\,M_\odot$ of gas onto a sink particle, we randomly sample a massive star with a mass between 9 and $120\,M_\odot$ from a Salpeter initial mass function (IMF, Salpeter 1955). We follow the stellar evolution of each of these massive stars according to the Ekström et al. (2012) tracks until they explode as supernovae. We refer to Gatto et al. (2016) for a detailed description of our cluster sink particles.

The simulations contain three different types of feedback from the formed star clusters. First, we include the radiative feedback from the massive stars in our stellar cluster sink particles. The stellar evolutionary tracks provide luminosities and effective temperatures as a function of stellar age, from which we compute the emitted spectrum. We use the `Fervent` code (Baczynski et al. 2015) to propagate the radiation from all sources individually in four different energy bins across the adaptive mesh using raytracing. The first energy bin $5.6\,\mathrm{eV} < E_{5.6} < 11.2\,\mathrm{eV}$ is responsible for the photoelectric heating of the ISM. Photons in the second energy bin $11.2\,\mathrm{eV} < E_{11.2} < 13.6\,\mathrm{eV}$ are energetic enough to photodissociate molecular hydrogen through the process $\mathrm{H_2} + \gamma_{11.2} \rightarrow \mathrm{H} + \mathrm{H}$. Photons from the third energy bin, $13.6\,\mathrm{eV} < E_{13.6} < 15.2\,\mathrm{eV}$, can photoionise atomic hydrogen via $\mathrm{H} + \gamma_{13.6} \rightarrow \mathrm{H^+} + \mathrm{e^-}$. Photons in the fourth bin, $15.2\,\mathrm{eV} < E_{15.2}$, can still photoionise atomic hydrogen, but they are also able to photoionise molecular hydrogen, $\mathrm{H_2} + \gamma_{15.2+} \rightarrow \mathrm{H_2^+} + \mathrm{e^-}$. Which one of these two processes occurs for a photon in this bin is decided based on the respective absorption cross sections if both forms of hydrogen are present in a given grid cell. The $\mathrm{H_2^+}$ ions formed by the latter process are assumed to immediately undergo dissociative recombination, resulting in the production of two hydrogen atoms. We do not include any form of radiation pressure. For more details on the complex photochemistry included in the `Fervent` code we refer to the method paper (Baczynski et al. 2015).

The second feedback process we include is the mechanical feedback from stellar winds. We take the mass-loss rates $\dot{M}_\mathrm{wind}$ directly from the Ekström et al. (2012) stellar evolutionary tracks. The computation of the wind terminal velocity v_wind depends on the evolutionary status of the stars. For OB stars and A supergiants, we use the scaling relations from Kudritzki & Puls (2000) and Markova & Puls (2008) on both sides of the bi-stability jump, and linearly interpolate in between (Puls et al. 2008). For WR stars, we linearly interpolate the observational data compiled by Crowther (2007), and for red supergiants we follow the scaling relation in van Loon (2006).

Within a given cluster, we add up the contributions of all cluster members. The total wind luminosity of a cluster with $N_\star$ stars is then

$$L_\mathrm{tot} = \frac{1}{2} \sum_{i=1}^{N_\star} \dot{M}_{\mathrm{wind},i} \times v_{\mathrm{wind},i}^2, \tag{1}$$

and the total mass-loss rate of the stellar cluster is

$$\dot{M}_\mathrm{tot} = \sum_{i=1}^{N_\star} \dot{M}_{\mathrm{wind},i}. \tag{2}$$

For each time step Δt, we add the mass $\dot{M}_\mathrm{tot} \times \Delta t$ to all cells within the wind injection region. We set the radius of this region equal to the sink accretion radius r_acc and distribute the injected mass equally among all cells within r_acc from the location of the sink centre. We assume that the wind is spherically symmetric and set the radial wind velocity of all cells within r_acc to

$$v_\mathrm{rad} = \sqrt{\frac{2 \times L_\mathrm{tot} \times \Delta t}{M_\mathrm{inj}}}, \tag{3}$$

where M_inj is the mass within the injection region. For more details on our implementation of stellar wind feedback, we refer to Gatto et al. (2016).

The third feedback process is the thermal feedback from supernova explosions. At the end of each massive star's life, we inject a thermal energy $E_\mathrm{SN} = 10^{51}\,\mathrm{erg}$ into a spherical region of radius r_acc around the sink particle. Additionally, we distribute the mass of the supernova progenitor equally over the cells in this volume. A detailed description of the supernova injection subgrid model is presented in Gatto et al. (2016).

Initially, we create a complex density structure by driving turbulence with an external forcing. This is necessary because otherwise the homogeneous disc would undergo global collapse and create a starburst. We inject kinetic energy with a flat power spectrum on the two largest modes in the plane of the disc, corresponding to the box size and half of the box size. We apply a natural mixture of 2:1 between solenoidal (divergence-free) and dilatational (curl-free) modes. The forcing field evolves according to an Ornstein-Uhlenbeck process (Eswaran & Pope 1988) with an autocorrelation time of 49 Myr, which corresponds to the crossing time in x and y directions. The amplitude of the forcing is adjusted such that a global, mass-weighted root-mean-square velocity of $10\,\mathrm{km\,s^{-1}}$ is attained. We switch off the forcing with the formation of the first sink particle, which happens at $t = 30\,\mathrm{Myr}$.

We use a notation for our simulations that is consistent with Gatto et al. (2016). Run FSN only includes feedback from supernova explosions, run FWSN incorporates feedback from winds and supernovae, and run FRWSN integrates feedback from radiation, winds and supernovae simultaneously. The simulations presented in this paper are summarised in Table 1. We have run all simulations for a total time $t_\mathrm{max} = 70\,\mathrm{Myr}$.

Table 1. Simulations

simulation name	supernova feedback	wind feedback	radiation feedback
FSN	yes	no	no
FWSN	yes	yes	no
FRWSN	yes	yes	yes

Overview of the simulations. We list the simulation names and the included feedback processes.

3 ENERGY BUDGET OF THE FEEDBACK PROCESSES

Before we start a differential analysis of the simulations, it is instructive to consider the energies associated with the

different forms of feedback. In Figure 1, we show the cumulative energy released by radiative and wind feedback for a star with 9, 12, 20 and 85 $M_\odot$. The stellar evolutionary tracks are identical to those shown in Figure 1 of Gatto et al. (2016).

The total radiation energy $E_{\rm rad}$ is computed from the stellar bolometric luminosities. It is 2 to 5 orders of magnitude larger than the wind energy $E_{\rm wind}$, dependent on the stellar mass. The higher the stellar mass, the smaller is the difference in the energies. But in contrast to $E_{\rm wind}$, $E_{\rm rad}$ is not fully deposited into the gas around the source. Photons with energies below 5.6 eV do not couple to the gas at all. More energetic photons only transfer energy to the gas in the presence of a sufficiently high column of absorbers. And even in this case, a significant fraction of energy is lost in overcoming the binding energies of the photochemical processes. Figure 1 also shows the maximum amount of energy that can be deposited into the gas within the `Fervent` energy bands, taking the binding energies into account and assuming high optical depths in all directions. For the 5.6 eV$< E_{5.6} <$ 11.2 eV energy band, we assume a photoelectric heating efficiency of 5 %, which is the largest value we expect to encounter in the dense ISM (Bakes & Tielens 1994).[1] In this case, the cumulative energies are orders of magnitude smaller than $E_{\rm rad}$, but still significantly larger than $E_{\rm wind}$. For the 9 and 12 $M_\odot$ stars, the majority of radiation energy is released by photoelectric heating, while for the 20 and 85 $M_\odot$ stars, photoionisation of H_2 and H are dominant. The cumulative energy available to photoelectric heating of a 12 $M_\odot$ star is comparable to the thermal energy injected with a supernova explosion. For a star as massive as 20 $M_\odot$, the energy available in each of the four energy bands is equivalent to the supernova explosion energy. If this radiation energy can be effectively absorbed by the surrounding medium, we can expect a significant impact of the radiative feedback on the ISM.

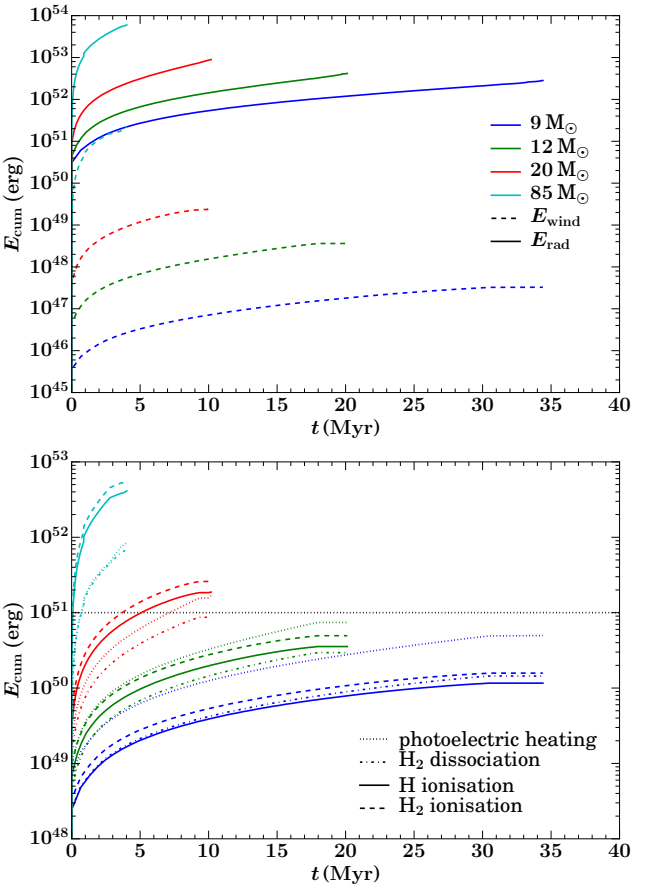

Figure 1. Cumulative energy released by different forms of feedback. *(top)* The total radiation energy $E_{\rm rad}$ (solid lines) is 2 to 5 orders of magnitude larger than the wind energy $E_{\rm wind}$ (dotted lines), dependent on the stellar mass. *(bottom)* The radiation energy that can potentially couple to the gas is much smaller, but can be comparable to the energy injected by a supernova explosion. The dominant photochemical processes are a function of stellar mass. The horizontal black dashed line indicates the supernova injection energy $E_{\rm SN} = 10^{51}$ erg.

4 QUALITATIVE DISCUSSION

The initial 30 Myr of evolution are identical for all simulations. The runs only start to differ when star formation and stellar feedback sets in. Figure 2 shows an example snapshot[2] from run FRWSN at $t = 57.2$ Myr. This particular point in time was chosen because it features a giant H II region, allowing us to judge the impact of radiative feedback in comparison to the other simulations without radiation. The picture shows edge-on (top) and face-on (bottom) density and temperature slices through the centre of the simulation box, projections of total gas density and of the different forms of hydrogen (H^+, H and H_2), and an image of the resulting Hα emission (from left to right). The generation of the Hα image is described in Section 10. The locations of the star cluster particles are indicated with white circles. In the vertical direction, we only show the inner 2 kpc of the total 10 kpc box height.

For comparison, Figure 3 shows run FWSN at the same time. It is clearly visible in the projections that the simulation box contains much less H^+. On the other hand, the temperature slices reveal that the ionised gas in the disc is much hotter on average, $T > 10^5$ K instead of $T \approx 10^4$ K for run FRWSN. As a result of both observations, the Hα emission is much reduced compared to run FRWSN (see Sections 10 and 11 for a detailed discussion). The number of sink particles in both simulations is very similar. The total disc scale height is also comparable.

In contrast, run FSN has a significantly larger disc scale height at the same time as the other two simulations, as we show in Figure 4. There is even more hot gas present than in run FWSN. Because of the larger column of ionised gas, run FSN has a slightly enhanced Hα emission compared to run FWSN. Since the simulation FSN is the only run that produces a volume filling fraction of hot gas in excess of 50 % (see Section 9), only this simulation drives a significant galactic outflow over an extended period of time (Gatto et al. 2016).

[1] In practice, the effective efficiency may be a factor of a few smaller than this. For example, in M31 it is around 2 % (Kapala et al., in prep.).
[2] An animated version of this figure can be found on the SILCC project website, http://hera.ph1.uni-koeln.de/~silcc/.

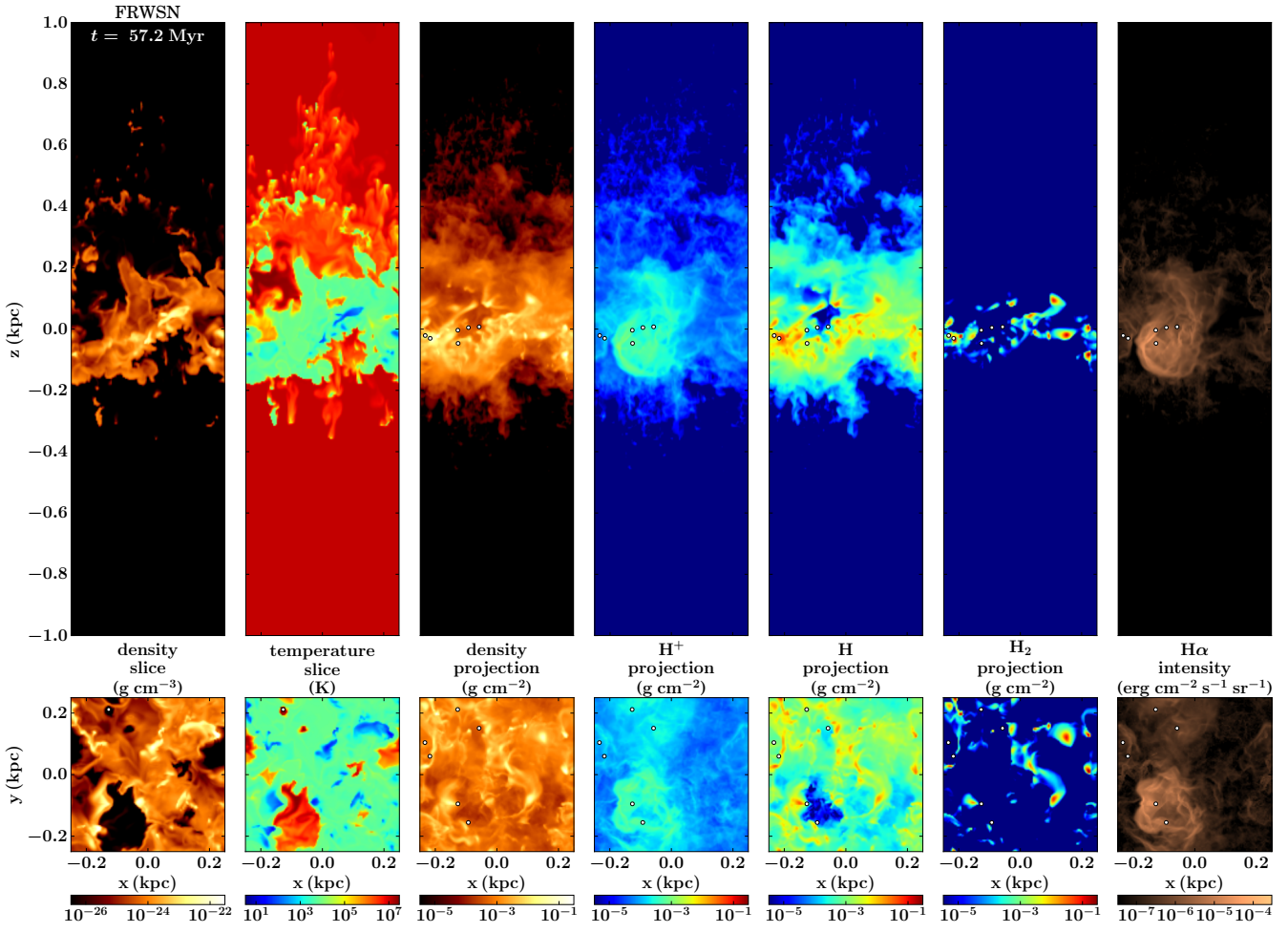

Figure 2. Example snapshot from run FRWSN including radiation, stellar winds and supernovae at $t = 57.2$ Myr. The picture shows edge-on (top) and face-on (bottom) density and temperature slices through the centre of the simulation box, projections of total gas density and of the different forms of hydrogen (H^+, H and H_2), and an image of the resulting Hα emission (from left to right). The locations of the star cluster particles are indicated with white circles. In the vertical direction, we only show the inner 2 kpc of the total 10 kpc box height. A movie of this simulation is available on the SILCC website (http://hera.ph1.uni-koeln.de/∼silcc/).

5 STAR CLUSTERS

Since the ISM is shaped by stellar feedback, it is key for understanding the ISM in our simulations to examine the stellar clusters that form. Star formation takes place by formation of new sink particles and by accretion onto already existing ones. As explained in Section 2, for each 120 $M_\odot$ of gas added to a sink particle, we select a new massive star by sampling from a Salpeter IMF. Figure 5 shows the SFR surface density $\Sigma_{\rm SFR}$ as a function of time t for all three simulations. We compute the SFRs in two different ways (see also Gatto et al. 2016). The instantaneous SFR is determined by summing the mass that is converted into stars over time intervals of 1 Myr. It describes the individual star formation events in the simulations.

However, when we want to compare the SFR in a simulation with the SFR measured in synthetic Hα images (Section 10), this is not the SFR we expect to observe. Instead, an OB star emits ionising radiation during its entire lifetime, not only when it has just formed. Therefore, we get a much better estimate of the observed SFR when we distribute the 120 $M_\odot$ of newly formed stars over the lifespan of the massive star associated with this cluster. The SFRs computed in this way are shown as solid lines in Figure 5. One can clearly see how this SFR declines after star formation events. This signifies the death of very massive stars ($M \geqslant 30\,M_\odot$) with short lifetimes (less than 7 Myr). In contrast, a 9 $M_\odot$ star lives for 35 Myr before it explodes as supernova. Because of the shape of the IMF, these stars at the lower end of the high-mass slope of the IMF are the most abundant stars in the clusters. Therefore, the SFR always remains positive at a significant level after the first star formation event, since these stars provide a floor to the observed SFR.

Comparing the three simulations in Figure 5, there are some notable differences. In run FSN, star formation events occur steadily from the onset of star formation at $t = 30$ Myr until we stop the simulation at $t = 70$ Myr. In contrast, runs FWSN and FRWSN display many fewer star formation events. As a result, the averaged SFR in these simulations is reduced by one order of magnitude compared to run FSN.

The reason for this behaviour is the self-regulation of star formation by early feedback (see also Gatto et al. 2016). Figure 6 shows for each sink particle formed in the three sim-

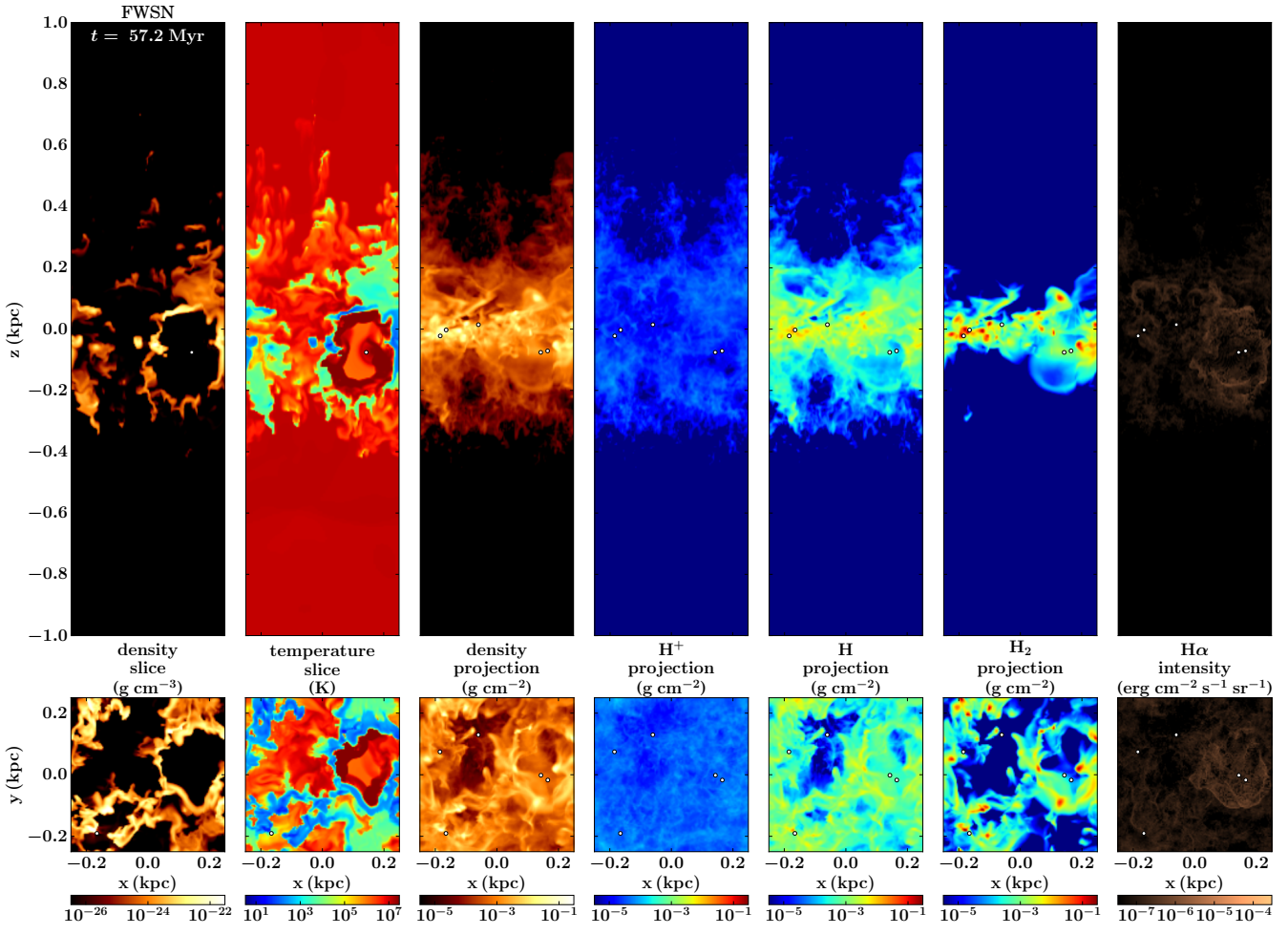

Figure 3. Same as Figure 2 for run FWSN including stellar winds and supernovae. A movie of this simulation is available on the SILCC website (http://hera.ph1.uni-koeln.de/∼silcc/).

ulations the time $t_{\rm sink,max}$ that it takes to reach its final mass $M_{\rm sink,max}$ versus $M_{\rm sink,max}$. In run FSN, the sink particles have final masses between 10^4 and $10^5\,{\rm M}_\odot$ and need some 10 Myr to reach this mass. For the first few Myr after their formation, the sink particles in this simulation can accrete unimpededly because no supernovae have exploded yet. In contrast, in run FWSN, stellar winds start blowing away the material close to the sink particle immediately after its formation. As a consequence, the final sink particle masses are reduced by one order of magnitude, and the typical timespan of sink particle accretion is reduced to only 0.1 to 1 Myr. In run FRWSN, where photoionisation feedback raises the thermal pressure by two orders of magnitude compared to the surrounding molecular gas, accretion is stopped even more efficiently. Here, the majority of sink particles have masses around $10^3\,{\rm M}_\odot$ and accrete for only 0.1 Myr.

It is important to note that both wind and radiation feedback are steady processes that commence with the first star formation event and only cease when all stars in the cluster are gone. Therefore, strong infall onto the sink particle is necessary to quench this feedback to the extent that accretion can continue for more than 1 Myr, or to facilitate a second episode of star formation after the sink particle already contains a substantial population of stars. In contrast, supernova feedback is highly intermittent. Therefore, in run FSN sink particles can accrete even when supernovae are already exploding. In this case, accretion continues during the time intervals between consecutive supernova explosions, when the gas has cooled sufficiently after a supernova injection.

We can compare our SFR surface density to the observational data of Leroy et al. (2008). For normal star-forming spiral galaxies with $\Sigma_{\rm gas} = 10\,{\rm M}_\odot\,{\rm pc}^{-2}$, the average SFR surface density is around $\Sigma_{\rm SFR} = 6\times10^{-3}\,{\rm M}_\odot\,{\rm yr}^{-1}\,{\rm kpc}^{-2}$, which corresponds to the Kennicutt-Schmidt value. However, the data shows a significant scatter around this number. Figure 7 displays the SFR surface density $\Sigma_{\rm SFR}$ for the three simulations as a function of time t. The plot also indicates a factor of three margin around the Kennicutt-Schmidt value, which is within the scatter in the Leroy et al. 2008 data for this $\Sigma_{\rm gas}$ (see also Figure 14). We find that run FSN is on the upper end of the margin, while runs FWSN and FRWSN are on the lower end. The time-averaged SFR in run FRWSN is slightly lower than in run FWSN, indicating that early feedback by radiation is only responsible for a small additional reduction on top of the already substantial lowering of the SFR by stellar winds. Since we do not have a control run with radiation but without winds, we cannot say

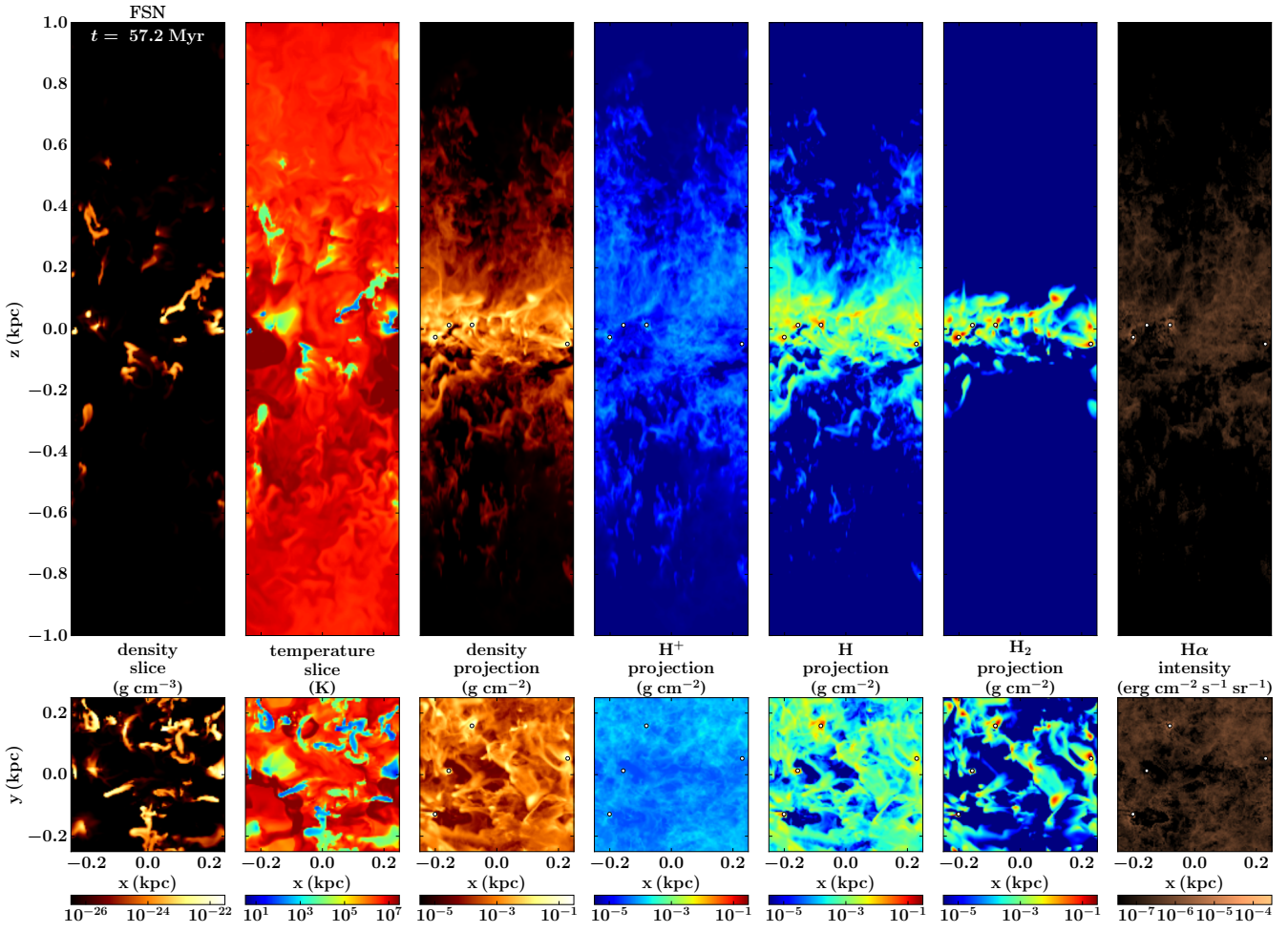

Figure 4. Same as Figure 2 for run FSN including only supernovae. A movie of this simulation is available on the SILCC website (http://hera.ph1.uni-koeln.de/∼silcc/).

whether the winds are essential here, or if radiation alone would have a comparable effect as the winds.

The reduced SFR in runs FWSN and FRWSN compared to run FSN has consequences for the stellar populations (star cluster sink particles) in the simulations. Figure 8 shows histograms of all stars formed during the three runs. The number counts for run FSN are elevated by a factor of 10 compared to the other two simulations. In particular, while run FSN has a substantial population of very massive stars with $M \geqslant 30\,\mathrm{M}_\odot$, runs FWSN and FRWSN only have very few such stars. However, since both wind and radiative energy output are a steep and highly non-linear function of stellar mass (compare Figure 1), this small population still dominates the amount of energy injected into the ISM. We quantify this effect in Section 6.

6 ENERGY INPUT

We can study the impact of the different forms of stellar feedback on the ISM by considering the associated energies. Figure 9 shows the cumulative energy injected by supernova explosions $E_{\mathrm{SN,cum}}$ as a function of time t for the three simulations. Since run FSN forms roughly ten times more stars than the simulations with early feedback FWSN and FRWSN, $E_{\mathrm{SN,cum}}$ is increased by a similar factor. As we have already seen, the SFR in runs FWSN and FRWSN does not differ much, and therefore $E_{\mathrm{SN,cum}}$ is comparable in these simulations, too.

Figure 9 also depicts the cumulative energy injected into the ISM by stellar winds $E_{\mathrm{wind,cum}}$. Here also, the simulations FWSN and FRWSN behave very similarly at all times. In both runs, $E_{\mathrm{wind,cum}}$ at the end of the simulation $t = 70\,\mathrm{Myr}$ is around $2 \times 10^{52}\,\mathrm{erg}$, which should be compared to $E_{\mathrm{SN,cum}}$ at that time, which is $10^{53}\,\mathrm{erg}$.

The impact of a supernova injection depends on the ambient density of the gas. Since we inject thermal energy with each supernova, the effect of an explosion grows with decreasing ambient density. Dense gas cools radiatively very quickly, whereas underdense gas stays hot for a long time. Figure 10 shows the cumulative distribution of supernovae as a function of the mean environmental density ρ_{SN} in which they explode, normalised to the total number of supernova explosions. In run FSN, essentially all supernovae go off at a mean density around $\rho_{\mathrm{SN}} = 3 \times 10^{-22}\,\mathrm{g\,cm^{-3}}$, which is two orders of magnitude lower than the threshold density for sink particle formation ρ_{thr}. In simulation FWSN, where stellar winds blow the dense gas out of the supernova injection

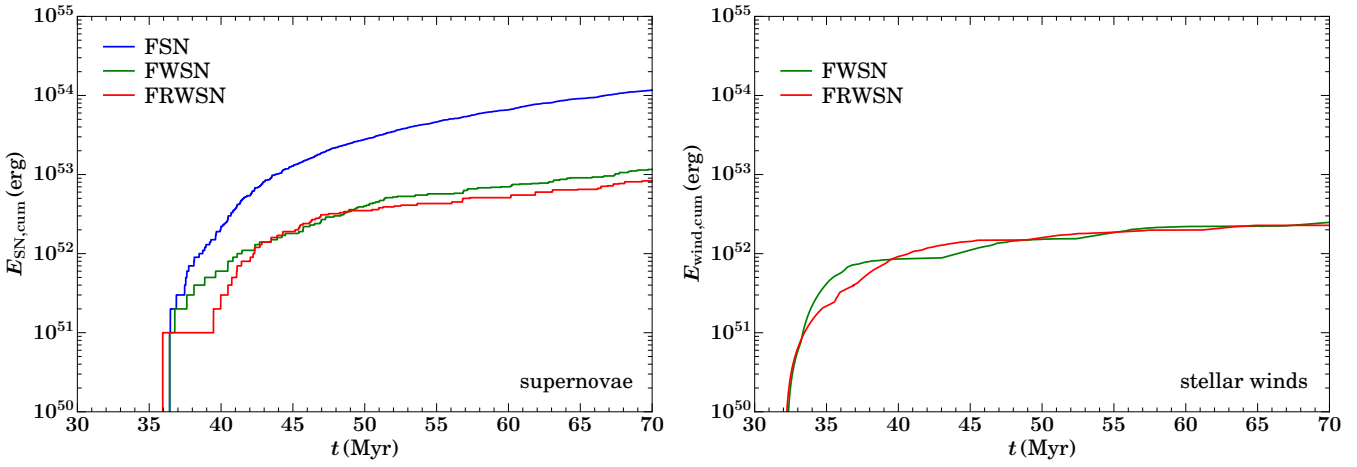

Figure 9. Cumulative energy injection by supernova explosions (left) and stellar winds (right) for the three simulations as a function of time. Runs FWSN and FRWSN have similar cluster sink properties and therefore similar energy injection statistics. The corresponding plot for radiation is shown in Figure 11.

region, the distribution function becomes much broader. The lowest mean density reached is only $\rho_{\rm SN} = 2 \times 10^{-26}\,{\rm g\,cm^{-3}}$, and the median of the distribution is $\rho_{\rm SN} = 10^{-25}\,{\rm g\,cm^{-3}}$. Therefore, half of all supernovae explode in very low-density gas. In run FRWSN, the distribution is similarly broad, but the median is only $\rho_{\rm SN} = 3 \times 10^{-26}\,{\rm g\,cm^{-3}}$ in this case. This is the effect of the additional photoevaporation flow in this simulation. Therefore, run FRWSN creates the largest amount of hot gas per supernova, followed by run FWSN and run FSN. On the other hand, run FRWSN has the smallest SFR.

The energy input by winds and supernovae should be compared with the energy released by the star clusters in the form of radiation in run FRWSN. Figure 11 displays the cumulative energy available to the different photochemical processes included in `Fervent`, computed in the same way as in Section 3. Already H_2 dissociation alone can impart more energy to the ISM than the supernova explosions, provided that this radiation is actually absorbed. The largest amount of energy can be transferred to the ISM via photoionisation heating, with a total amount of 1.2×10^{54} erg at $t = 70\,{\rm Myr}$ with H_2 and H photoionisation combined. Of course, neither photoelectric heating nor photoionisation or photodissociation can produce $10^6\,{\rm K}$ hot gas like winds or supernovae. But considering the total energy budget in the ISM, the contribution from radiation is very substantial. Even if only one tenth of all available radiation energy can be tapped by the material, this energy still exceeds the combined energy input by winds and supernovae.

In Figure 11, we also show the instantaneous luminosity of the different processes as a function of time. The curves show several jumps where the radiative output suddenly drops by orders of magnitude. The origin of this variability is the strong dependence of the luminosity on stellar mass (compare Figure 1). As discussed in Section 5, the star clusters of run FRWSN contain only very few stars with $M \geqslant 30\,{\rm M_\odot}$ (see Figure 8). These stars dominate the cluster luminosity as long as they are present, but they live only for a few Myr. After they have exploded as supernovae, only less massive stars survive that produce a lower luminosity.

Figure 12 illustrates this effect. It shows the radiative energy output associated with the ionisation of atomic hydrogen as a function of time. We plot the energy emitted by less massive stars with $M < 30\,{\rm M_\odot}$, very massive stars with $M \geqslant 30\,{\rm M_\odot}$, and the sum of the two. The cumulative plot shows that the former contribute only 20 % to the total radiation energy. The plot of the instantaneous luminosity emitted by the clusters reveals that very massive stars with $M \geqslant 30\,{\rm M_\odot}$ dominate the radiative output by an order of magnitude or more. When these stars disappear, the curve drops to a floor value produced by the less massive stars with $M < 30\,{\rm M_\odot}$ (see e.g. da Silva et al. 2014; Krumholz et al. 2015, for a detailed analysis of the effect of stochastic stellar populations on estimated SFRs).

7 MASS FRACTIONS

The different stellar populations and energy input in the three simulations are reflected in the resulting ISM. Figure 13 shows the time evolution of the total mass and of the mass fractions of atomic, ionised and molecular hydrogen. In run FSN, about 10 % of the initial gas mass gets accreted onto sink particles during the simulation. For run FWSN, it is only 1 %, and for run FRWSN even less. These results are consistent with the trend in the SFRs for the three simulations (compare Figure 7).

Interestingly, the evolution of the atomic hydrogen mass fraction is almost identical in runs FSN and FWSN, with a value around 40 %. Simulation FRWSN, however, has a mass fraction of atomic hydrogen around 70 %. This is due to the effect of photodissociation, which converts molecular into atomic gas.

The mass fraction of ionised hydrogen starts to grow monotonically 10 Myr after the onset of star formation from 1 % to 7 % in run FSN. This is the result of the supernova explosions, which produce an increasing amount of ionised gas. Run FWSN has a roughly constant ionised hydrogen mass fraction of 2 %. Due to the reduced SFR in this simulation, many fewer supernovae explode compared to run FSN, and the additional collisional ionisation by stellar wind

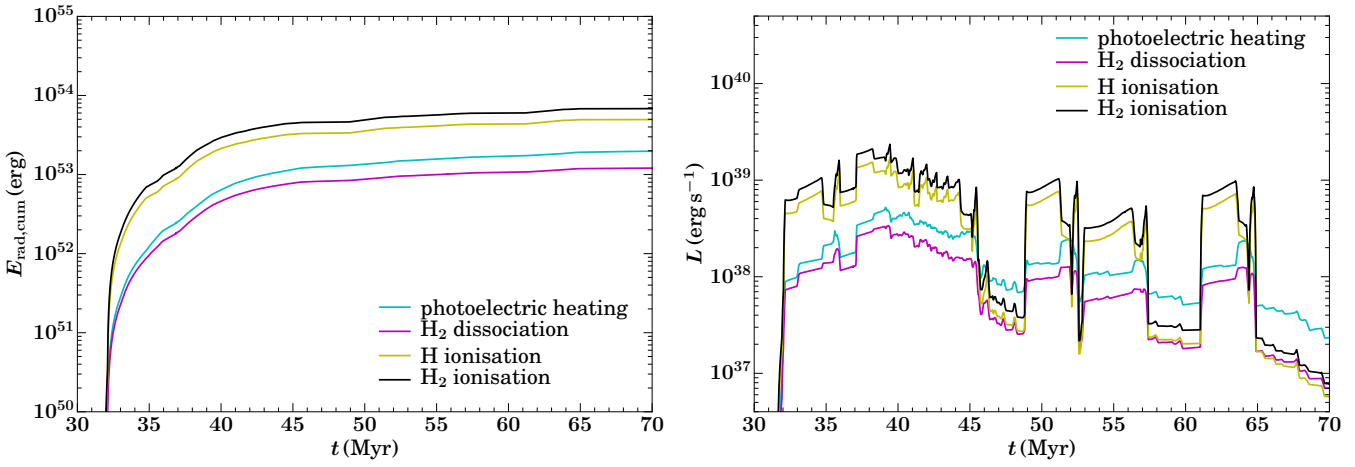

Figure 11. Left: Cumulative radiation energy output in the different photochemical processes of all stellar clusters in run FRWSN. Right: Instantaneous luminosity as a function of time. The total energy output is dominated by photoionisation of H_2 and H, followed by photoelectric heating and H_2 dissociation.

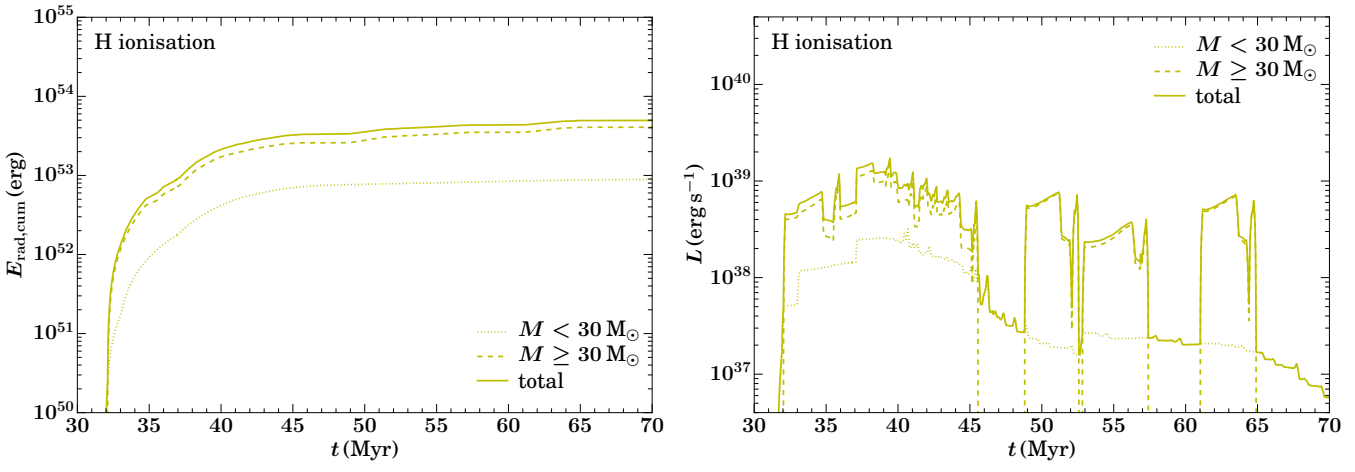

Figure 12. Same as Figure 11, but for atomic hydrogen ionisation only. We have separated the contributions from stars with masses $M < 30\,{\rm M}_\odot$ (dotted) and $M \geqslant 30\,{\rm M}_\odot$ (dashed) to the total (solid).

feedback cannot compensate for this effect. The ionised hydrogen mass fraction of run FRWSN oscillates between 3 % and 10 % as a function of time. These oscillations are very closely correlated with the variability in the radiative output from the star clusters (compare Figure 11). This clearly demonstrates that photoionisation from stellar radiation is the primary source of ionised gas in this simulation, with supernovae and winds contributing only a negligible amount.

The molecular hydrogen mass fraction of run FSN drops from 60 % to 40 % from 40 Myr onwards. The delay of 10 Myr between the onset of star formation and the reduction of the molecular hydrogen mass fraction suggests that it is due to supernova feedback, since the evolution of the atomic and ionised hydrogen mass fractions show a similar behaviour. In contrast, if this reduction was primarily due to accretion of molecular gas onto the sink particles, one would not expect such a delay. For run FWSN, the molecular hydrogen mass fraction stays at around 60 %. In run FRWSN, the molecular hydrogen mass fraction oscillates around a value of 20 %. These oscillations are again indicative of photoevaporation processes caused by the stellar irradiation of the molecular clouds.

8 DEPLETION TIME

Since we dynamically form H_2 in the simulations, it is interesting to check whether the relation between the molecular gas surface density Σ_{H_2} and the SFR surface density $\Sigma_{\rm SFR}$ obtained in the simulations is in agreement with observations. The ratio of these two quantities is the depletion time $t_{\rm dep} = \Sigma_{H_2}/\Sigma_{\rm SFR}$. Using $\Sigma_{\rm SFR}$ from Figure 7 and the instantaneous Σ_{H_2} measured in face-on projections of the disc, we can plot $t_{\rm dep}$ as a function of time for the three simulations. The result is shown in Figure 14.

In the data analysed by Bigiel et al. (2008), the average depletion time is $t_{\rm dep} = 2\,{\rm Gyr}$. Only the run FRWSN reproduces this value. The SFR in run FSN is too high for the amount of molecular gas present, and run FWSN has too much molecular gas for such a small SFR. Compared

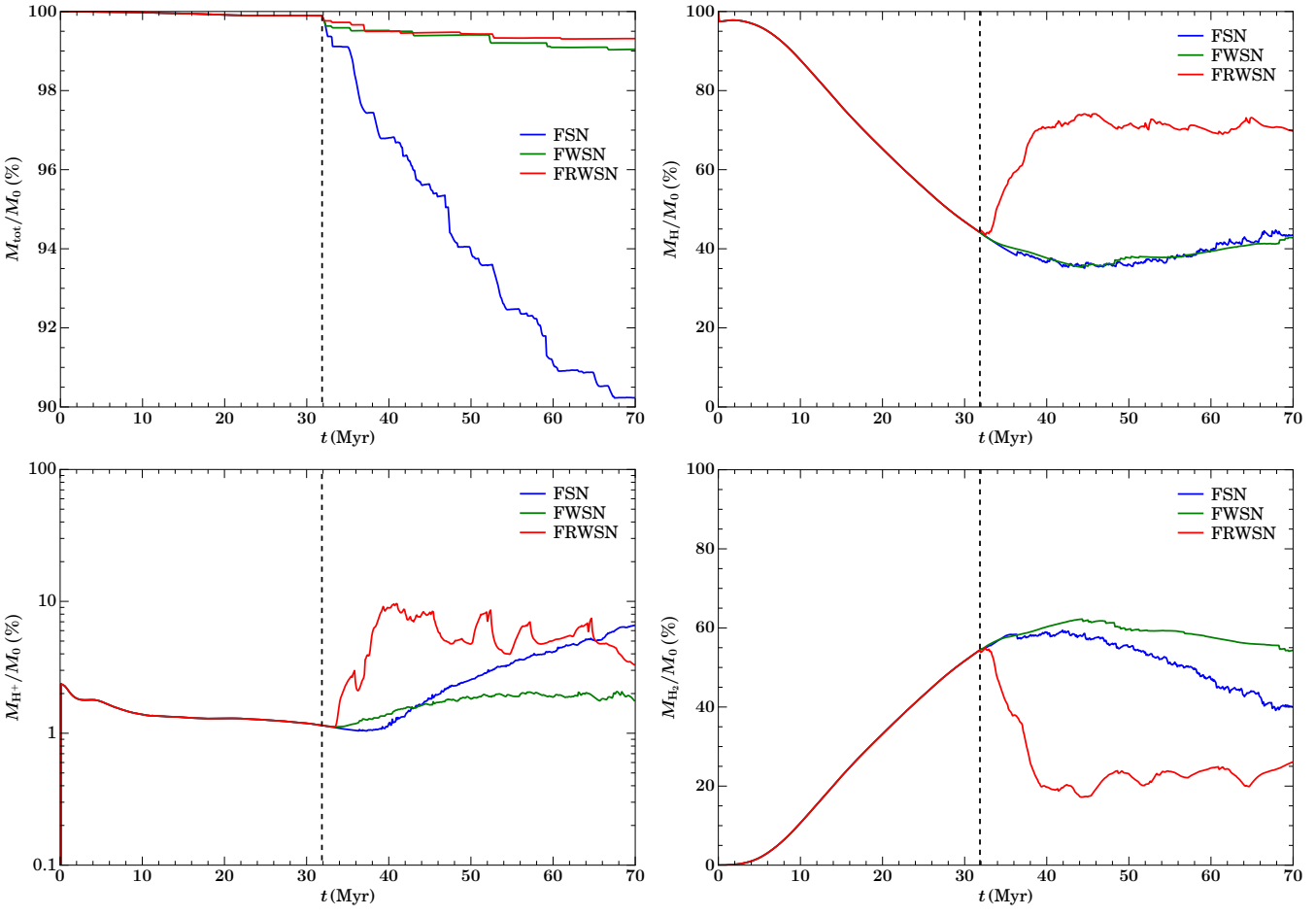

Figure 13. Total mass and mass fraction of atomic, ionised and molecular hydrogen as a function of time t for all simulations (from top left to bottom right). All masses are normalised to M_0, the total mass at $t = 0$. The drop of the total mass over time is due to accretion of gas by sink particles. The vertical dashed line marks the onset of star formation.

to run FWSN, radiation reduces $\Sigma_{\rm H_2}$ more than $\Sigma_{\rm SFR}$, and $t_{\rm dep}$ falls on the observed value.

Figure 14 also shows $\Sigma_{\rm SFR}$ versus $\Sigma_{\rm H_2}$ for the three simulations. We have omitted the data prior to $t = 40\,{\rm Myr}$, because this is the time required for the H_2 mass fraction in run FRWSN to converge and become relatively constant (compare Figure 13). For most of the time, run FRWSN is within the observational scatter of 0.8 Gyr around the average depletion time in the data of Bigiel et al. (2008). The curve for run FRWSN in this plot nicely illustrates the effect of star formation self-regulation.

It is also interesting to consider the relation between $\Sigma_{\rm SFR}$ and $\Sigma_{\rm H+H_2}$ instead of $\Sigma_{\rm H_2}$. In Figure 14 we plot the data from Leroy et al. (2008) together with the time-averaged quantities from $t = 40\,{\rm Myr}$ to $t = 70\,{\rm Myr}$ for the three simulations. As already remarked in Section 5, our values are within the scatter of the observational data. Run FSN is near the upper end in $\Sigma_{\rm SFR}$, but runs FWSN and FRWSN are in the middle of the scatter for their $\Sigma_{\rm H+H_2}$.

9 VOLUME FILLING FRACTIONS

Another interesting property of the ISM is the volume filling fraction of the different ISM phases. Following Gatto et al. (2016), we use these temperature cuts to define the phases:

(i) molecular phase ($T \leqslant 30\,{\rm K}$),
(ii) cold phase ($30 < T \leqslant 300\,{\rm K}$),
(iii) warm phase ($300 < T \leqslant 8000\,{\rm K}$),
(iv) warm-hot phase ($8000 \leqslant T \leqslant 3 \times 10^5\,{\rm K}$),
(v) hot phase ($T > 3 \times 10^5\,{\rm K}$).

Note that molecular here refers to the CO-bright molecular gas. CO-dark molecular gas has a much broader temperature distribution (see e.g. Glover & Smith 2016), and in our simulations much of it is located in our cold phase (see Walch et al. 2015; Peters et al. 2016, for more on this point). In our analysis, we ignore the molecular phase since it is not well resolved in our simulations. The time evolution of the volume filling fractions of the cold, warm, warm-hot and hot phases are shown in Figure 15. We restrict the computation of the volume filling fraction to the inner disc region with $|z| \leqslant 100\,{\rm pc}$.

The volume filling fraction for the cold phase shows only little variation with time in all cases and falls between 2 % and 9 %. The situation is similar for the warm-hot phase,

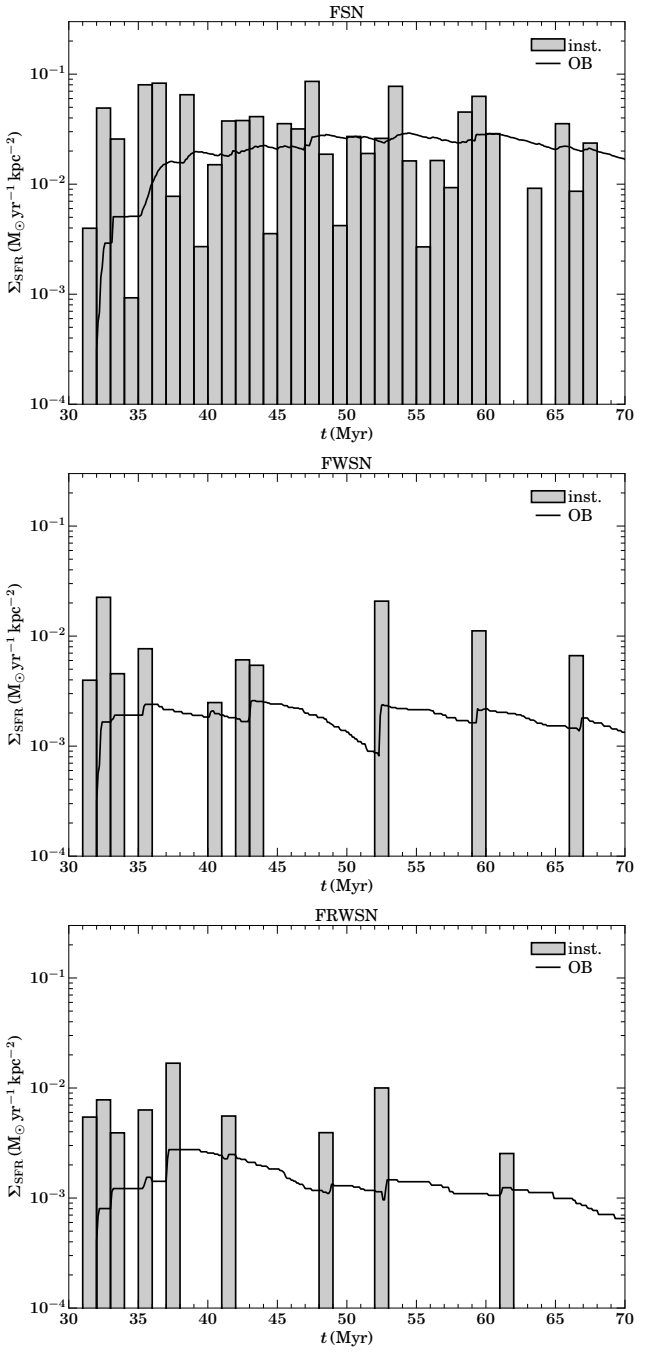

Figure 5. SFR surface density $\Sigma_{\rm SFR}$ as a function of time t for runs FSN, FWSN and FRWSN (from top to bottom). The panels show the instantaneous star formation events, binned over intervals of 1 Myr, and SFRs distributed over the OB stars' lifetimes (solid lines).

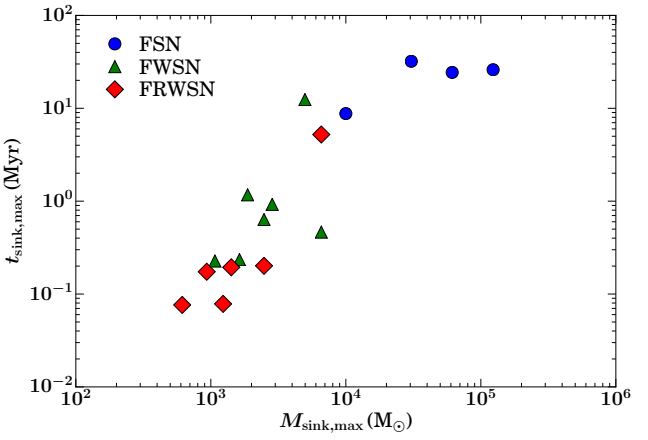

Figure 6. Time $t_{\rm sink,max}$ it takes for a sink particle to reach its final mass $M_{\rm sink,max}$ vs. $M_{\rm sink,max}$ for the three simulations.

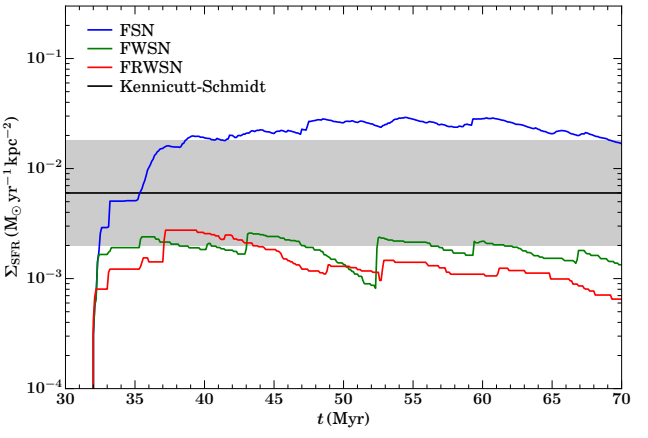

Figure 7. SFR surface density $\Sigma_{\rm SFR}$ as a function of time t in the simulations. The black line indicates the Kennicutt-Schmidt value, and the grey band a factor of three uncertainty.

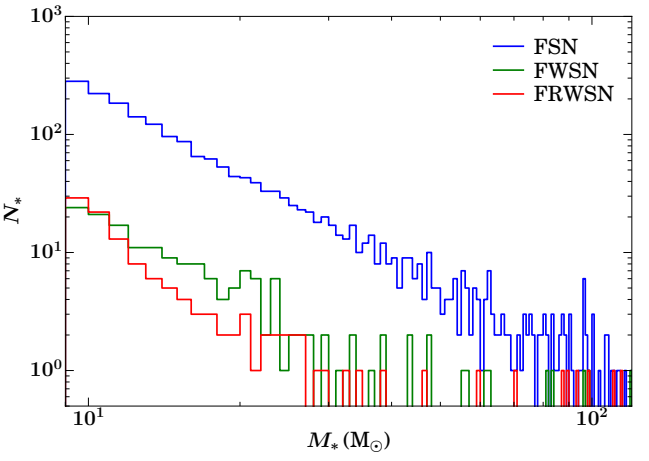

Figure 8. Histograms of all massive stars formed during the three simulations.

where the volume filling fraction lies between 8 % and 11 %. Here, there is no clear trend between the simulations. This is understandable since the warm-hot phase is thermally unstable, so we only see gas in a transient state.

The situation is different for the other two phases, which show a behaviour that is approximately opposite to each other. Run FSN produces a volume filling fraction of the hot phase of 85 % and of the warm phase of 10 %. Run FWSN,

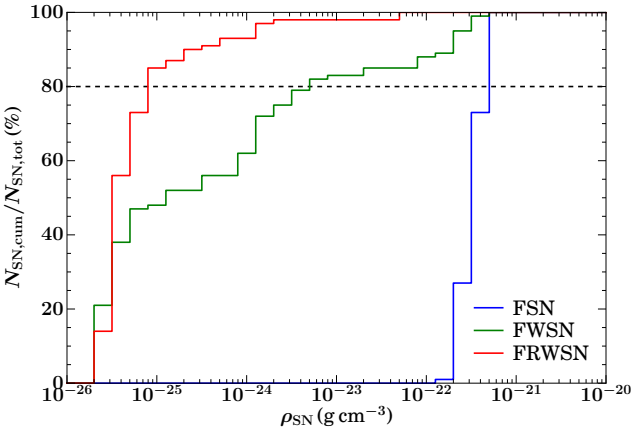

Figure 10. Normalised cumulative distribution of supernovae as a function of the mean environmental density in which they explode for the three simulations. The inclusion of winds reduces the ambient density of 80 % of the supernova explosions from less than $\sim 10^{-22}\,\mathrm{g\,cm^{-3}}$ to less than $\sim 10^{-23}\,\mathrm{g\,cm^{-3}}$, which is further dramatically reduced to less than $\sim 10^{-25}\,\mathrm{g\,cm^{-3}}$ by radiation.

with a factor of ten smaller SFR, produces a volume filling fraction of the hot phase of only 50 %, while the volume filling fraction of warm phase increases to 30 %. The hot phase volume filling fraction in run FRWSN, with a factor of two smaller SFR, varies around 25 %, and in the warm phase around 75 %. A comparison between the simulations is difficult because one has to separate the effects of the different SFR from the impact of the various forms of stellar feedback. But the differences between the simulations FWSN and FRWSN appear too large to be primarily a result of the smaller SFR in run FRWSN. Instead, they are likely the result of the inclusion of radiative feedback in run FRWSN. Photoionisation produces a lot more ionised gas than is present in run FWSN (compare Figure 13), which then radiatively cools and enters the warm phase. This is why the volume filling fraction in the warm phase is enhanced, at the cost of the hot phase volume filling fraction. Gatto et al. (2016) have shown that a volume filling fraction in excess of 50 % in the hot phase is necessary to drive galactic outflows (cosmic rays modify this picture, see e.g. Peters et al. 2015; Girichidis et al. 2016; Simpson et al. 2016). This is consistent with our finding that only run FSN launches an outflow that leaves the inner ±1 kpc of the box in the vertical direction during the simulation.

Our results can be compared with the observation-based models for the ISM phase volume filling fractions presented in Kalberla & Kerp (2009). In the inner 100 pc, they find a volume filling fraction in the cold phase of 18 %, in the warm phase of 42 %, in the warm-hot phase of 20 %, and in the hot phase of 17 % (their Figure 11). These values are shown as crosses in Figure 15. The cold phase is the only phase where run FRWSN does not reproduce the observed value, in the simulation it is too small by a factor of three. The observed volume filling fraction of the warm-hot phase is matched by all simulations. But for the warm and hot phases, the simulation with radiation is the only one that approaches the oberved values. The other simulations underestimate the warm and overerstimate the hot phase.

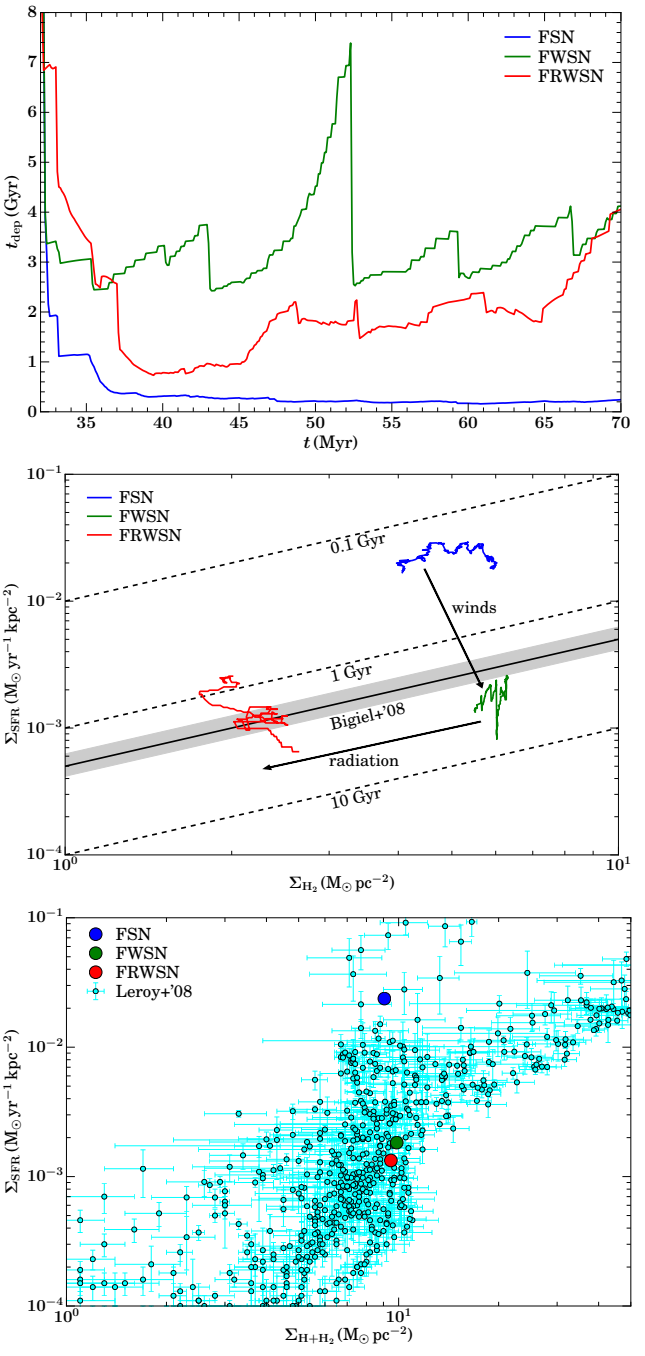

Figure 14. Top: Depletion time $t_{\rm dep} = \Sigma_{\rm H_2}/\Sigma_{\rm SFR}$ for the three simulations as a function of time t. Middle: Plot of $\Sigma_{\rm SFR}$ versus $\Sigma_{\rm H_2}$ for the three simulations for all snaphots after $t = 40\,\mathrm{Myr}$. The dashed lines show constant depletion times of 0.1, 1 and 10 Gyr (from top to bottom). The solid line represents the average value $t_{\rm dep} = 2\,\mathrm{Gyr}$ from Bigiel et al. (2008), and the grey band marks the observational scatter of 0.8 Gyr in their data. Bottom: Plot of $\Sigma_{\rm SFR}$ and $\Sigma_{\rm H+H_2}$ time-averaged from $t = 40\,\mathrm{Myr}$ to $t = 70\,\mathrm{Myr}$ for the three simulations together with the data from Leroy et al. (2008).

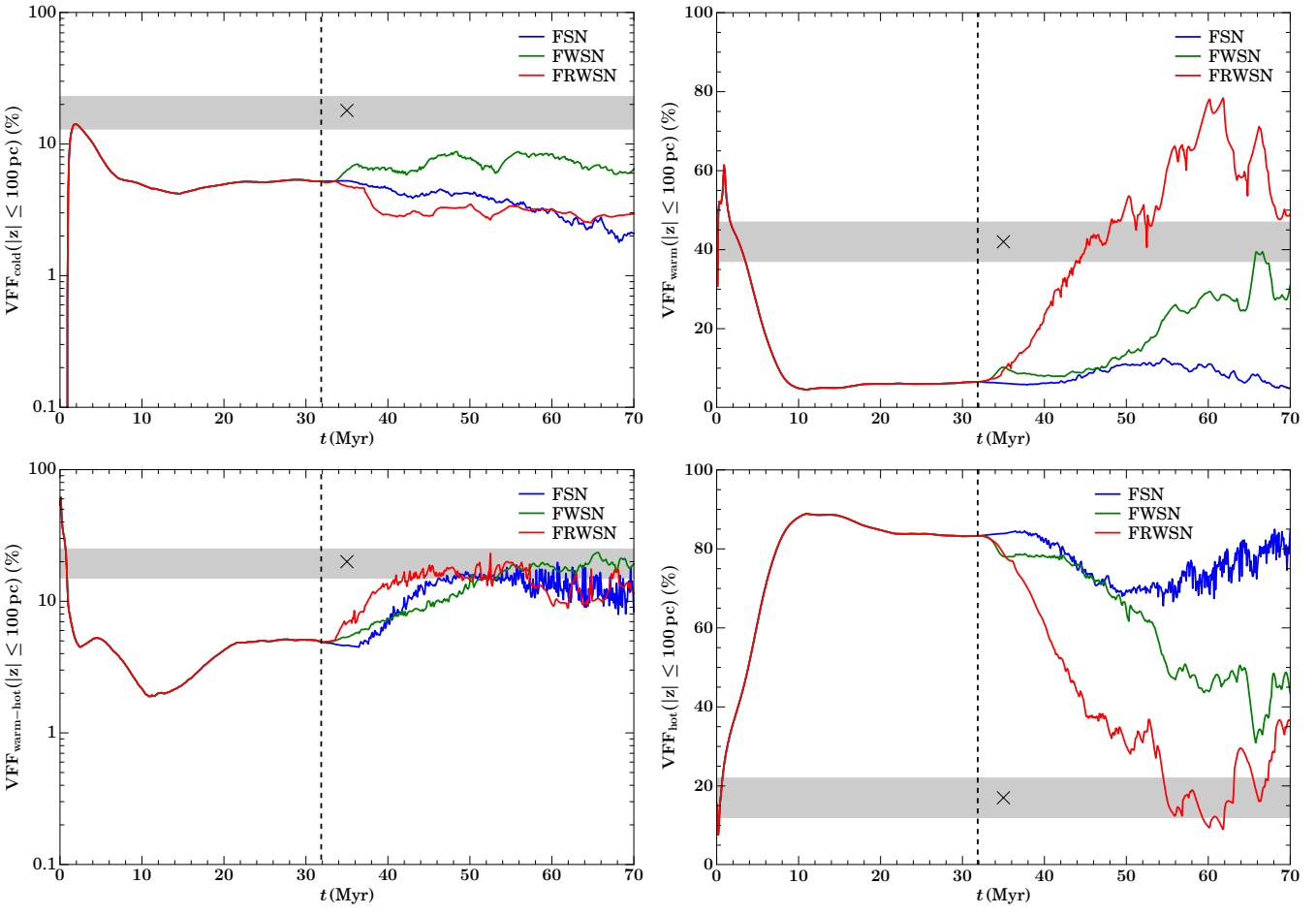

Figure 15. Volume filling fractions within the volume $|z| \leqslant 100\,\mathrm{pc}$ for the cold, warm, warm-hot and hot phase as a function of time t for all simulations (from top left to bottom right). The vertical dashed line marks the onset of star formation. Crosses and grey bands are the data of Kalberla & Kerp (2009).

10 Hα MAPS

The ionised gas in the ISM can be observed with the Hα recombination radiation emitted during the Balmer transition $n = 3 \rightarrow n = 2$. The Hα radiation is mostly emitted from gas with $T \approx 10^4\,\mathrm{K}$, which is primarily photoionised gas. The gas that is shock-ionised by winds and supernovae is typically too hot to be observed in Hα, but can become visible as the shocks cool down. Because of the close connection between Hα emission and H II regions from massive stars, Hα is an important SFR tracer. Our simulations allow us to investigate systematic errors in the calibration of SFR measurements in Hα, and in particular to quantify the contamination of the Hα flux from shock emission.

To this end, we produce synthetic Hα observations of our simulation box. Two processes contribute to the emission of Hα radiation. The first one is the recombination of ionised hydrogen with a free electron. We describe the emissivity caused by radiative recombination following Eq. (9) of Dong & Draine (2011) as

$$j_{\mathrm{H}\alpha,\mathrm{R}} = 2.82{\times}10^{-26}\,T_4^{-0.942-0.031\ln(T_4)}\,n_\mathrm{e} n_{\mathrm{H}^+}\,\frac{\mathrm{erg}}{\mathrm{cm^3\,s\,sr}}, \quad (4)$$

where n_e and n_{H^+} are the number densities of electrons and protons, respectively, and $T_4 = T/10^4\,\mathrm{K}$ with the gas temperature T. The second contribution comes from collisional excitation of neutral hydrogen by free electrons. We follow Kim et al. (2013) and set

$$j_{\mathrm{H}\alpha,\mathrm{C}} = \frac{1.30\times10^{-17}}{4\pi}\,\frac{\Gamma_{13}(T)}{\sqrt{T}}\,\exp\left(\frac{-12.1\,\mathrm{eV}}{k_\mathrm{B}T}\right) n_\mathrm{e} n_\mathrm{H}\,\frac{\mathrm{erg}}{\mathrm{cm^3\,s\,sr}} \quad (5)$$

according to their Eq. (6), with Boltzmann's constant k_B, the number density of neutral hydrogen n_H and the Maxwellian-averaged effective collision strength

$$\Gamma_{13}(T) = 0.35{-}2.62{\times}10^{-7}T{-}8.15{\times}10^{-11}T^2{+}6.19{\times}10^{-15}T^3, \quad (6)$$

for $4,000\,\mathrm{K} \leqslant T \leqslant 25,000\,\mathrm{K}$ and

$$\Gamma_{13}(T) = 0.276{+}4.99{\times}10^{-6}T{-}8.85{\times}10^{-12}T^2{+}7.18{\times}10^{-18}T^3, \quad (7)$$

for $25,000\,\mathrm{K} < T \leqslant 500,000\,\mathrm{K}$. The formulas for the collision strength are based on polynomial interpolation through data by Aggarwal (1983). In the subsequent discussion, we will look at these two contributions separately as well as at their sum $j_{\mathrm{H}\alpha} = j_{\mathrm{H}\alpha,\mathrm{R}} + j_{\mathrm{H}\alpha,\mathrm{C}}$. For simplicity, we assume $n_\mathrm{e} = n_{\mathrm{H}^+}$ during post-processing. Deviations from this (due to e.g. the presence of helium) will change our values by less than 20%.

Both emissivities $j_{\mathrm{H}\alpha,\mathrm{R}}$ and $j_{\mathrm{H}\alpha,\mathrm{C}}$ have a similar

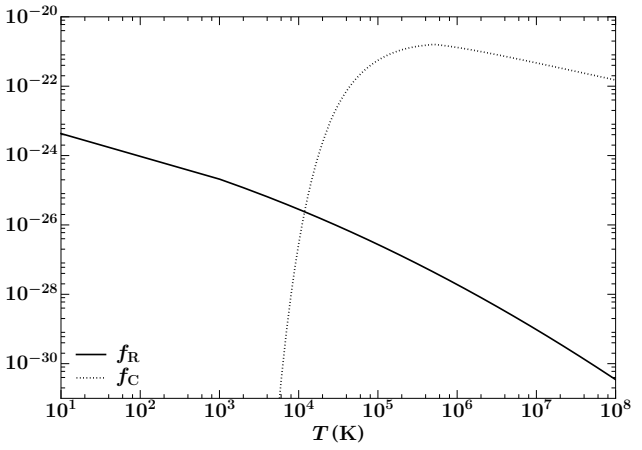

Figure 16. Density-independent prefactors $f_{\rm R}$ and $f_{\rm C}$ of radiative recombination emission and collisional excitation emission, respectively, as a function of temperature T.

functional form. Radiative recombination emission is proportional to the product $n_{\rm e} n_{\rm H^+}$ with a temperature-dependent prefactor $f_{\rm R}(T)$, whereas collisional excitation emission is proportional to $n_{\rm e} n_{\rm H}$ with prefactor $f_{\rm C}(T)$. The temperature-dependence of these proportionality factors $f_{\rm R}(T)$ and $f_{\rm C}(T)$, which are defined by the formulas (4) and (5), respectively, is shown in Figure 16. Assuming that the products of number densities are of a similar magnitude, radiative recombination dominates at temperatures $T \ll 10^4\,{\rm K}$, whereas collisional excitation becomes dominant at $T \gg 10^4\,{\rm K}$. The fact that Hα emission primarily originates from gas with $T \approx 10^4\,{\rm K}$ is because of the temperature-dependence of the different ionisation stages of hydrogen. The abundance of $n_{\rm H}$ drops substantially above $T \approx 10^4\,{\rm K}$, reducing the magnitude of $j_{{\rm H}\alpha,{\rm C}}$. Likewise, the abundance of $n_{\rm H^+}$ decreases signifantly below $T \approx 10^4\,{\rm K}$, which diminishes $j_{{\rm H}\alpha,{\rm R}}$.

We integrate the emissivities along parallel rays through the simulation box, neglecting scattering and absorption by intervening dust. For the projection along the z-axis, which mimics a patch of a face-on view of a Milky Way-type galaxy, we compute the total Hα luminosity by integrating over the entire image. We will also separately consider the Hα luminosity from radiative recombination emission and from collisional excitation emission only.

11 Hα LUMINOSITY SURFACE DENSITY

In Figure 17 we show the Hα luminosity surface density $S_{{\rm H}\alpha}$ for the face-on images for the three simulations as a function of time t. This data is identical to the maps shown in the movies corresponding to the Figures 2, 3 and 4, respectively. We plot the contribution from radiative recombination emission, collisional excitation emission, and the total emission.

In run FSN, $S_{{\rm H}\alpha}$ grows with time after the onset of the supernova explosions. Superimposed on this average growth is a series of very pronounced spikes of the Hα emission that boost the Hα luminosity by many orders of magnitude. These spikes are produced by the injection of thermal energy into the dense gas inside the sink particle radius during a supernova explosion, which produces a large amount of collisional ionisation. These injections are visible as bright spots around the sink particles in the Hα panels of the corresponding movie. Collisional excitation emission dominates over radiative recombination emission by a factor of 2–3 on average.

In run FWSN, stellar winds evacuate the sink particle volume before the first supernova explosions commence. Thus, the thermal energy injection during supernova explosions create much less collisional ionisation, and as a consequence the spikes in $S_{{\rm H}\alpha}$ disappear. We already know that in this simulation, stellar feedback does not produce much ionised gas (compare Figure 13), and therefore $S_{{\rm H}\alpha}$ only increases by a factor of a few after the onset of star formation, but remains roughly constant throughout the simulation. Again, collisional excitation emission dominates over radiative recombination emission by a small factor.

For run FRWSN, the situation is very different. We have already seen in Figure 13 that the radiative feedback boosts the amount of ionised gas by the formation of H II regions. Figure 17 demonstrates that, as a consequence, $S_{{\rm H}\alpha}$ increases by one order of magnitude compared to run FWSN. Interestingly, the flux coming from collisional excitation emission remains approximately at the same level as in run FWSN, whereas the rise in the Hα flux is entirely due to a much enhanced radiative recombination emission. This is the radiation coming from the H II regions. As soon as the first H II regions form, radiative recombination emission always dominates over collisional excitation emission, but the difference can vary from a factor of only 2 up to more than an order of magnitude. If we identify collisional excitation emission with shocks and radiative recombination emission with H II regions, then shocks can contribute at most 30 % to the total Hα flux, but typically less than 10 %. The total Hα flux varies in the same way as the mass fraction of ionised gas because of the oscillations in the radiative energy output (compare Figure 11).

12 STAR FORMATION RATE CALIBRATION

Measurements of the Hα flux are routinely used as SFR tracers. To this end, the Hα luminosity surface density $S_{{\rm H}\alpha}$ is converted into an SFR surface density $\Sigma_{\rm SFR}$. The typical conversion factors between $S_{{\rm H}\alpha}$ and $\Sigma_{\rm SFR}$ used in the literature only differ by a factor of 2. We consider the following calibrations:

- $\Sigma_{\rm SFR} = 8.9 \times 10^{-42}\, S_{{\rm H}\alpha}$ (Kennicutt 1983),
- $\Sigma_{\rm SFR} = 7.9 \times 10^{-42}\, S_{{\rm H}\alpha}$ (Kennicutt 1998),
- $\Sigma_{\rm SFR} = 5.3 \times 10^{-42}\, S_{{\rm H}\alpha}$ (Calzetti et al. 2007),
- $\Sigma_{\rm SFR} = 5.45 \times 10^{-42}\, S_{{\rm H}\alpha}$ (Calzetti et al. 2010).

In these formulae, $S_{{\rm H}\alpha}$ is assumed to be given in units $\mathrm{erg\,s^{-1}\,kpc^{-2}}$, so that $\Sigma_{\rm SFR}$ has units $\mathrm{M_\odot\,yr^{-1}\,kpc^{-2}}$.

SFR calibrations including Hα (Kennicutt 1998) connect the observed emssion of galaxies to the reprocessed light from a population of young massive stars by the ISM. These calibrations rely on a variety of assumptions, including the IMF, and number of ionising photons absorbed by dust, which do not produce Hα. The rates used here are derived using extinction-corrected Hα fluxes, with assumptions about the geometry of sources and dust (Calzetti et al. 2007). A future improvement of our analysis will include

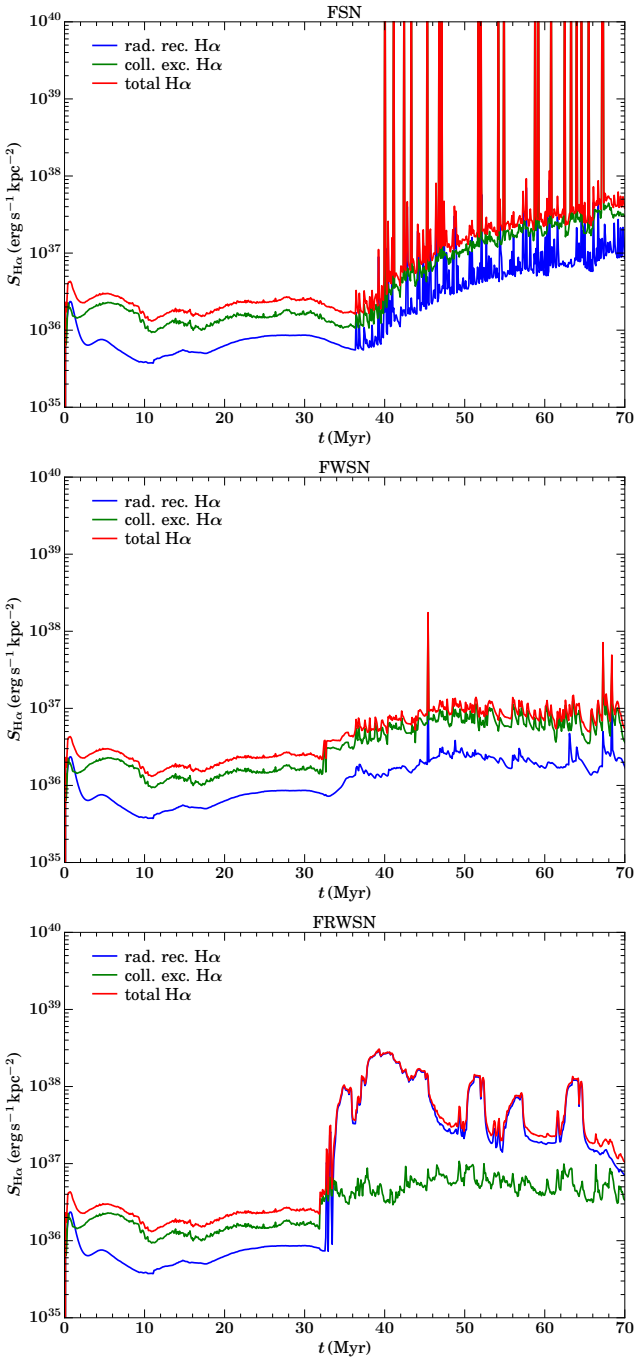

Figure 17. Hα luminosity surface density $S_{H\alpha}$ for all simulations as a function of time t. The plots show the contribution from radiative recombination emission, collisional excitation emission and the total emission.

dust absorption of ionising radiation, which would lower the calculated emission per unit of SFR. The column densities of this simulation are similar to the galaxies in Boquien et al. (2016). There they found the amount of Lyman continuum photons absorbed by dust to be only 10 %.

Figure 18 shows the SFR measured in Hα using these calibrations for run FRWSN together with the true SFR, which we have already computed in Section 5 (compare Figure 7). As discussed previously, the true SFR was derived

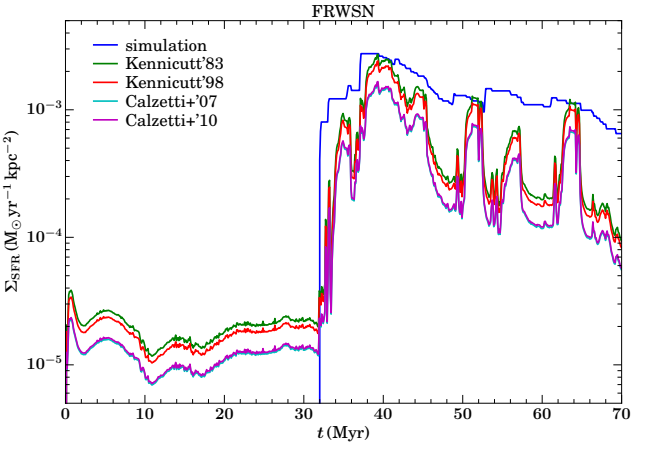

Figure 18. SFR surface density Σ_{SFR} measured in the simulation and derived via various Hα SFR calibrations as a function of time t for run FRWSN.

by distributing the mass of a newly born cluster over the associated massive star's lifespan, thereby taking into account the period over which it emits ionising radiation. This SFR contrasts with the naive theoretical SFR shown in Figure 5, which simply bins star formation events in 1 Myr intervals and does not take the finite stellar lifetime that affects observational SFR measurements into account. We therefore expect a good agreement between our true SFR and the SFR measured in Hα.

Indeed, after the onset of star formation, the observed and the true SFR follow each other closely. However, after 45 Myr the Hα flux drops by an order of magnitude, whereas the true SFR remains roughly constant. In the following, we see a series of oscillations in the observed SFR that has no correspondence in the true SFR. We have already found that the origin of these oscillations is the death of very massive stars with $M \geqslant 30\,M_\odot$ that dominate the stellar luminosities, but have short lifetimes (compare Figure 12). The true SFR does not oscillate because most stars in the clusters are less massive and therefore long-lived (compare Figure 8). This plot therefore demonstrates that Hα measurements of the SFR are only accurate when very massive stars are present. Less massive stars do not produce enough ionising flux to produce an Hα emission that matches their SFR. In this case, the Hα measurement can underestimate the SFR by an order of magnitude, independent of the calibration used. This is an important systematic error for Hα measurements of the SFR (see also da Silva et al. 2014; Hony et al. 2015).

13 CONCLUSIONS

We present simulations of the multi-phase ISM that simultaneously include stellar feedback in the form of supernovae, stellar winds and radiation. These chemo-radiation-hydrodynamical simulations are part of the SILCC project and extend previous simulations of self-regulated star formation by winds and supernovae (Gatto et al. 2016) by radiative feedback in the form of photoelectric heating, photodissociation and photoionisation from star clusters using the `Fervent` code (Baczynski et al. 2015).

We find that photoionisation feedback contributes to the regulation of star formation by an increase in thermal pressure that the accretion flow around the star cluster must overcome to continue growing. Therefore, a simulation with feedback by radiation, winds and supernovae has on average lower-mass clusters that accrete for a shorter period of time compared to a simulation with only wind and supernova feedback. As a consequence, the SFR is reduced by a factor of 2 in this case. For the same reason, supernovae explode in an environment with a lower mean density in the presence of radiation.

We find that, for this simulation, photoionisation heating is the dominant energy source in the ISM and that it exceeds the energy input from supernovae by one and from winds by two orders of magnitude. All photochemical processes can individually impart more energy into the ISM than supernovae, provided that this radiation is absorbed by the material. The cluster luminosities are highly variable with time because they are dominated by very massive stars ($M \geqslant 30\,\mathrm{M}_\odot$) with lifetimes of only a few Myr.

The presence of radiative feedback significantly affects the mass fractions of the different chemical states of hydrogen. The mass fractions of atomic and ionised hydrogen increase whereas the molecular hydrogen mass fraction drops. Photoionisation by star clusters is the dominant source of ionised gas in the ISM. This ionised gas then cools radiatively and produces a much enhanced volume filling fraction of the warm phase and a substantial reduction of the hot phase volume filling fraction compared to simulations without radiation. This is essential to match the observed volume filling fractions of the warm and hot phases. The simulation with radiation naturally exhibits a depletion time that is in agreement with observations, while the other simulations fail to do so.

The time variability of the cluster luminosities has important consequences for SFR measurements in Hα. We find that the SFR observed in Hα only matches the true SFR when very massive stars are present in the clusters. Less massive stars do not produce enough ionising radiation to create an Hα flux that matches their SFR. The Hα measurement then underestimates the SFR by up to an order of magnitude, and this result is independent of the calibration used. Shock emission typically contributes less than 10 % to the total Hα flux, but can go up to 30 %.

ACKNOWLEDGEMENTS

All simulations have been performed on the Odin and Hydra clusters hosted by the Max Planck Computing & Data Facility (http://www.mpcdf.mpg.de/). TP, TN, SW, SCOG, PG and RSK acknowledge the *Deutsche Forschungsgemeinschaft (DFG)* for funding through the SPP 1573 "The Physics of the Interstellar Medium". TN acknowledges support by the DFG cluster of excellence "Origin and structure of the Universe". SW acknowledges funding by the Bonn-Cologne-Graduate School, by SFB 956 "The conditions and impact of star formation", and from the European Research Council under the European Community's Framework Programme FP8 via the ERC Starting Grant RADFEEDBACK (project number 679852). SCOG and RSK acknowledge support from the DFG via SFB 881 "The Milky Way System" (sub-projects B1, B2 and B8). RSK acknowledges support from the European Research Council under the European Community's Seventh Framework Programme (FP7/2007-2013) via the ERC Advanced Grant STARLIGHT (project number 339177). RW acknowledges support by project 15-06012S of the Czech Science Foundation and the institutional project RVO: 67985815. The software used in this work was developed in part by the DOE NNSA ASC- and DOE Office of Science ASCR-supported Flash Center for Computational Science at the University of Chicago. The data analysis was partially carried out with the `yt` software (Turk et al. 2011).

REFERENCES

Aggarwal, K. M. 1983, MNRAS, 202, 15P
Baczynski, C., Glover, S. C. O., & Klessen, R. S. 2015, MNRAS, 454, 380
Bakes, E. L. O., & Tielens, A. G. G. M. 1994, ApJ, 427, 822
Bigiel, F., Leroy, A., Walter, F., et al. 2008, AJ, 136, 2846
Boquien, M., Kennicutt, R., Calzetti, D., et al. 2016, A&A, 591, A6
Bouchut, F., Klingenberg, C., & Waagan, K. 2007, Numerische Mathematik, 108, 7
Calzetti, D., Kennicutt, R. C., Engelbracht, C. W., et al. 2007, ApJ, 666, 870
Calzetti, D., Wu, S.-Y., Hong, S., et al. 2010, ApJ, 714, 1256
Clark, P. C., Glover, S. C. O., & Klessen, R. S. 2012, MNRAS, 420, 745
Crowther, P. A. 2007, ARA&A, 45, 177
da Silva, R. L., Fumagalli, M., & Krumholz, M. R. 2014, MNRAS, 444, 3275
Dale, J. E., Bonnell, I. A., Clarke, C. J., & Bate, M. R. 2005, MNRAS, 358, 291
de Avillez, M. A., & Breitschwerdt, D. 2004, A&A, 425, 899
Dong, R., & Draine, B. T. 2011, ApJ, 727, 35
Draine, B. T. 1978, ApJS, 36, 595
Dubey, A., Antypas, K., Ganapathy, M. K., et al. 2009, Parallel Computing, 35, 512
Ekström, S., Georgy, C., Eggenberger, P., et al. 2012, A&A, 537, A146
Eswaran, V., & Pope, S. B. 1988, Computers & Fluids, 16, 257
Federrath, C., Banerjee, R., Clark, P. C., & Klessen, R. S. 2010, ApJ, 713, 269
Förster Schreiber, N. M., Genzel, R., Bouché, N., et al. 2009, ApJ, 706, 1364
Fryxell, B., Olson, K., Ricker, P., et al. 2000, ApJS, 131, 273
Gatto, A., Walch, S., Mac Low, M.-M., et al. 2015, MNRAS, 449, 1057
Gatto, A., Walch, S., Naab, T., et al. 2016, arXiv:1606.05346
Geen, S., Rosdahl, J., Blaizot, J., Devriendt, J., & Slyz, A. 2015, MNRAS, 448, 3248
Girichidis, P., Naab, T., Walch, S., et al. 2016, ApJ, 816, L19

Girichidis, P., Walch, S., Naab, T., et al. 2016, MNRAS, 456, 3432
Glover, S. C. O., & Clark, P. C. 2012, MNRAS, 421, 116
Glover, S. C. O., Federrath, C., Mac Low, M.-M., & Klessen, R. S. 2010, MNRAS, 404, 2
Glover, S. C. O., & Mac Low, M.-M. 2007a, ApJS, 169, 239
—. 2007b, ApJ, 659, 1317
Glover, S. C. O., & Smith, R. J. 2016, MNRAS, 462, 3011
Gnat, O., & Ferland, G. J. 2012, ApJS, 199, 20
Goldsmith, P. F., & Langer, W. D. 1978, ApJ, 222, 881
Gritschneder, M., Naab, T., Walch, S., Burkert, A., & Heitsch, F. 2009, ApJ, 694, L26
Habing, H. J. 1968, Bull. Astron. Inst. Netherlands, 19, 421
Henley, D. B., Shelton, R. L., Kwak, K., Hill, A. S., & Mac Low, M.-M. 2015, ApJ, 800, 102
Hony, S., Gouliermis, D. A., Galliano, F., et al. 2015, MNRAS, 448, 1847
Joung, M. K. R., & Mac Low, M.-M. 2006, ApJ, 653, 1266
Kalberla, P. M. W., & Kerp, J. 2009, ARA&A, 47, 27
Kennicutt, Jr., R. C. 1983, ApJ, 272, 54
Kennicutt, Jr., R. C. 1998, ApJ, 498, 541
Kim, C.-G., & Ostriker, E. C. 2015a, ApJ, 802, 99
—. 2015b, ApJ, 815, 67
Kim, J.-h., Krumholz, M. R., Wise, J. H., et al. 2013, ApJ, 779, 8
Korpi, M. J., Brandenburg, A., Shukurov, A., Tuominen, I., & Nordlund, Å. 1999, ApJ, 514, L99
Krumholz, M. R., Fumagalli, M., da Silva, R. L., Rendahl, T., & Parra, J. 2015, MNRAS, 452, 1447
Kudritzki, R.-P., & Puls, J. 2000, ARA&A, 38, 613
Leroy, A. K., Walter, F., Brinks, E., et al. 2008, AJ, 136, 2782
Mac Low, M.-M., & Klessen, R. S. 2004, Reviews of Modern Physics, 76, 125
Markova, N., & Puls, J. 2008, A&A, 478, 823
Martizzi, D., Faucher-Giguère, C.-A., & Quataert, E. 2015, MNRAS, 450, 504
Nelson, R. P., & Langer, W. D. 1997, ApJ, 482, 796
Ostriker, J. P., & McKee, C. F. 1988, Reviews of Modern Physics, 60, 1
Peters, T., Banerjee, R., & Klessen, R. S. 2008, Physica Scripta, T132, 014026
Peters, T., Banerjee, R., Klessen, R. S., et al. 2010, ApJ, 711, 1017
Peters, T., Girichidis, P., Gatto, A., et al. 2015, ApJ, 813, L27
Peters, T., Zhukovska, S., Naab, T., et al. 2016, submitted to MNRAS
Puls, J., Vink, J. S., & Najarro, F. 2008, A&A Rev., 16, 209
Salpeter, E. E. 1955, ApJ, 121, 161
Simpson, C. M., Pakmor, R., Marinacci, F., et al. 2016, ApJ, 827, L29
Tacconi, L. J., Genzel, R., Neri, R., et al. 2010, Nature, 463, 781
Turk, M. J., Smith, B. D., Oishi, J. S., et al. 2011, ApJS, 192, 9
van Loon, J. T. 2006, in Stellar Evolution at low Metallicity: Mass Loss, Explosions, Cosmology, ed. H. J. G. L. M. Lamers, N. Langer, T. Nugis, & K. Annuk (San Francisco: ASP), 211
Waagan, K. 2009, J. Comput. Phys., 228, 8609
Waagan, K., Federrath, C., & Klingenberg, C. 2011, J. Comput. Phys., 230, 3331
Walch, S., & Naab, T. 2015, MNRAS, 451, 2757
Walch, S., Girichidis, P., Naab, T., et al. 2015, MNRAS, 454, 238
Walch, S. K., Whitworth, A. P., Bisbas, T., Wünsch, R., & Hubber, D. 2012, MNRAS, 427, 625
Weaver, R., McCray, R., Castor, J., Shapiro, P., & Moore, R. 1977, ApJ, 218, 377
Whitworth, A. 1979, MNRAS, 186, 59
Wolfire, M. G., Hollenbach, D., McKee, C. F., Tielens, A. G. G. M., & Bakes, E. L. O. 1995, ApJ, 443, 152